Dissertation
submitted to the
Combined Faculties for the Natural Sciences and for Mathematics
of the Ruperto-Carola University of Heidelberg, Germany
for the degree of
Doctor of Natural Sciences

Put forward by
Dipl.-Phys. Stefan Sellner
Born in Mannheim
Oral examination: 18. December 2013

Simulations, Optimizations, and Microdosimetric Measurements of Beam Quality for Heavy-Ion Tumor Therapy

A charged (particle) issue.

Referees: Prof. Dr. Joachim Ullrich
Prof. Dr. Wolfgang Schlegel

Contents

Simulationen, Optimierungen und mikrodosimetrische Messungen der Strahlqualität für die Schwerionen-Krebstherapie

Krebstherapie mit Teilchenstrahlen bietet die Möglichkeit, den Tumor noch gezielter zu treffen als mit Röntgenstrahlen, wodurch umliegendes, gesundes Gewebe besser geschont wird und so die Erfolgswahrscheinlichkeit der Therapie erhöht werden kann. Die Anwendung dieser Technik bedarf allerdings weitreichender Kenntnisse nicht nur über die physikalischen Aspekte, sondern auch über die biologische Wirksamkeit der Strahlung in Gewebe. Diese Wirksamkeit hängt kompliziert von vielen physikalischen wie auch biologischen Faktoren ab und muss mit komplexen Modellen berechnet werden; es gibt jedoch einen engeren Zusammenhang mit dem linearen Energietransfer (LET), also dem Maß für die Konzentration der Energieabgabe eines Teilchens entlang seiner Spur: steigt der LET (bis zu einer gewissen Schwelle), so steigt auch die biologische Wirksamkeit. Ferner können wegen Sauerstoffarmut strahlenresistente Tumorzellen ebenfalls mit einem hohen LET wirksam abgetötet werden. Der LET selbst hängt jedoch wiederum von der kinetischen Energie des Teilchens ab, genau wie die Strahlendosis. Dies macht eine simultane Optimierung beider Größen nur bedingt möglich, eine Methode wird jedoch in dieser Arbeit vorgestellt, die sich das Konzept der Dosisrampen zunutze macht. Es werden Beispiele für Teilchenstrahlung bestehend aus Protonen, Kohlenstoffionen oder Antiprotonen vorgestellt und gezeigt, dass sich mit den heute verfügbaren und zugelassenen Mitteln der klinischen Dosisplanung Bereiche mit hohem LET vorteilhaft im Tumorvolumen verteilen lassen, ohne die Dosisverteilung nennenswert zu beeinflussen.

Im experimentellen Teil der Arbeit geht es um die Anwendung eines gewebeäquivalenten Proportionalzählers (engl. tissue-equivalent proportional counter, TEPC), um mikroskopische Dosisverteilungen in linealer Energie, d. h. die Fluktuationen in der Energiekonzentration in subzellulären Größenordnungen, zu bestimmen. Das Maß der Fluktuationen und die Höhe der Energiekonzentration stehen ebenfalls, wie der LET, mit der biologischen Wirksamkeit in Zusammenhang. In den vorgestellten Messungen wird überprüft, ob sich zwei gängige Varianten der Teilchenstrahlapplikation maßgeblich in ihren Dosisverteilungen in linealer Energie unterscheiden, sodass sich unter Umständen aus den Unterschieden ein unterschiedlicher biologischer Effekt ableiten lässt.

Simulations, Optimizations, and Microdosimetric Measurements of Beam Quality for Heavy-Ion Tumor Therapy

Tumor radiotherapy with charged particles offers superior properties in covering the tumor with radiation dose, while sparing the surrounding, healthy tissue better than standard X-rays. Thus, the success of the therapy is potentially increased. However, the application of this technique necessitates not only profound knowledge about its physical aspects, such as the uncertainties in the range of the particles which need to be taken into account in the therapy planning stage. In addition to the physical aspects, the biological effectiveness of particle radiation needs to be thoroughly understood. The effectiveness depends on many physical as well as biological quantities and is determined involving complicated models. Though, there is a close relation with the linear energy transfer (LET), i. e. the measure of the local concentration of energy deposition along a particle's track. The higher the LET (up to a certain limit), the higher the biological effect. Furthermore, radiation resistant cells, e. g. due to a lack of oxygenation, can be effectively killed with radiation that has a high LET. The LET itself depends on the kinetic energy of the particle, just like the dose, which makes a simultaneous optimization of dose and LET possible only under some circumstances. However, this work presents a method that makes use of the dose ramp concept to beneficially re-distribute areas with high LET using protons, carbon ions and antiprotons, respectively, without notably influencing the dose distribution.

In the experimental part of this work, a tissue-equivalent proportional counter (TEPC) is used to measure microscopic dose distributions in lineal energy, i. e. fluctuations of the energy concentration on sub-cellular length scales. The extent of these fluctuations as well as the magnitude of the energy concentration have, like the LET, an influence on the biological effect. In the measurements presented here it is assessed if there is a significant change in the dose distributions in lineal energy when comparing two methods of particle beam application to determine a potential impact on the biological effect.

1 Radiation Cancer Therapy

The uncontrolled growth of tissue is called cancer, i. e. malignant neoplasm. It is one of the most frequent causes of death, e. g. 25 % of all deaths in Germany were due to cancer in 2010 [1]. Remarkably, in 2008, about 54 % of all diagnosed cancers have been cured in Germany [2]. Neoplasms can be divided into benign tumors that are growing only slowly and threaten the organism mainly by their space consumption, while malignant tumors infiltrate neighboring tissue and can spread into the whole organism by the lymphatic and blood system. Further sub-divisions and information can be found in [3] (English) and [4] (German).

Tumors can be treated by means of surgery, medication (chemotherapy), and radiation therapy (external or internal), with the treatment chosen according to the tumor type, stage, and grade. Benign tumors are often treated by a combination of surgery and radiation therapy, while the therapy of malignant tumors most often includes chemotherapy because of its ability to metastatize into the whole organism.

Radiation therapy is defined as the treatment of malignant tissue with ionizing radiation. Other methods using non-ionizing irradiation are e.g. microwave or heat, light, ultra sound, and UV therapy. Ionizing radiation can be applied by means of teletherapy, where the radiation source is outside the body of the patient or by implanting radiation sources into or situating them very close to the target tissue (brachytherapy). Some more basic information about cancer and its therapy is given in this chapter.

1.1 Cancer treatment with ionizing radiation

Only two years after their discovery by W. C. Röntgen in 1895, X-rays have been used to irradiate tumors. Later, also neutrons, electrons, gamma rays from ^{60}Co, X-rays from electron bremsstrahlung, pions, protons and heavier ions were successfully

introduced. Today, the largest fraction of patients (about 1 million in the USA in 2004 [5]) is treated with X-rays resulting from bremsstrahlung of electrons with kinetic energies in the range between 6 and 23 MeV. Less than 1 % of the patients elegible for radiation therapy receive particle beam treatment (between 2012 and 2013, 5761 patients were treated with protons in the USA)[1] at least as part of their therapy.

The most prominent physical difference of the various irradiation techniques is the depth-dose distribution, i. e. the deposition pattern of energy to unit masses of the surrounding matter in dependence of the penetration depth. While photons show, after a build-up region of several millimeters, an exponential decay of deposited energy, charged particles deposit little energy as long as their kinetic energy is high, and a large amount at the end of their range, resulting in the so-called Bragg peak (cf. fig. 1.2). The average energy loss of a charged particle per unit path length traveled depends on the particle's kinetic energy and is also a property of the material traversed. It is called stopping power (SP) and can be expressed as a sum of three physical processes: The collision stopping power, which is the energy lost in inelastic collisions with the target's electrons, radiative losses due to bremsstrahlung, and the energy transferred to target nuclei in elastic collisions:

$$SP = -\left[\left(\frac{\mathrm{d}E}{\mathrm{d}x}\right)_{\mathrm{col}} + \left(\frac{\mathrm{d}E}{\mathrm{d}x}\right)_{\mathrm{brems}} + \left(\frac{\mathrm{d}E}{\mathrm{d}x}\right)_{\mathrm{nuc}}\right] \tag{1.1}$$

The collision stopping power is the dominant one for charged particles heavier than electrons and has first been described by Bethe [7]. The second term is only relevant for electrons that lose a considerable amount of their energy by bremsstrahlung. Because the bremsstrahlung cross section depends on the inverse square of the projectile's mass, it becomes irrelevant for protons or heavier ions. The last term becomes significant only for very low projectile energies (it is larger than 1 % only for protons with less than 20 keV energy in water, cf. [8]).

The formula for the collision stopping power, including the extension for slow as well as highly relativistic particles is given in eq. 1.2.

[1] the number was calculated from the yearly patient number statistics published by the Particle Therapy Cooperative Group, PTCOG, taking only proton therapy centers in the USA into account [6].

$$SP_{\text{col}} = -\left(\frac{\mathrm{d}E}{\mathrm{d}x}\right)_{\text{col}} = \frac{4\pi n z_{eff}^2}{m_e c^2 \beta^2} \cdot \left(\frac{e^2}{4\pi\varepsilon_0}\right)^2 \cdot \left[\ln\left(\frac{2m_e c^2 \beta^2}{I(1-\beta^2)}\right) - \beta^2 - \frac{C}{Z} - \frac{\delta}{2}\right] \quad (1.2)$$

SP, the stopping power, is the mean loss of energy $\mathrm{d}E$ of a particle on a length $\mathrm{d}x$ traveled. $n = \frac{Z \cdot \rho}{A \cdot u}$ is the electron density (Z and A being charge and mass number of the target nuclei, ρ the density and u the atomic mass unit), $m_e c^2$ the electron rest energy, z_{eff} the effective charge and $\beta = v/c$ the velocity of the beam particle. The effective charge can be described with the Barkas formula and differs from the atomic number only for small velocities. e is the charge constant, ε_0 the vacuum perittivity. I in the logarithmic term represents the mean ionization potential of the target, which is either measured and tabulated or often roughly approximated by $I = 10\,\text{eV} \cdot Z$. C and δ are the shell and density correction, respectively. While the shell correction only accounts for corrections for very low kinetic energies, where the projectile velocity is in the order of or lower than the target electron velocity, the density correction includes the dielectric polarization of dense media and becomes relevant for kinetic energies much larger than the therapeutic range. More information as well as tabulated values for the stopping power in the therapeutic energy range can be found in ICRU Report 49 [8] for protons and alpha particles and in ICRU Report 73 [9] for particles heavier than helium, respectively.

As the particle range depends on the particle's initial energy, many pristine Bragg peaks with different depths are superimposed to achieve a constant high dose throughout the tumor's depth. This is called spread-out Bragg peak (SOBP) and its construction with pristine peaks is shown in fig. 1.1.

Calculated examples of depth-dose distribution for protons and carbon ions in comparison with photons can be seen in fig. 1.2. The stong decrease of energy deposition after the Bragg peak and the higher dose in the target region compared to the dose in front make particles excellent candidates for a better dose conformation to the tumor than photons and, therefore, a better treatment outcome. For heavier ions, this effect is further enhanced in the lateral direction, i. e. perpendicular to the beam axis, because of reduced angular scattering.

In addition to these purely physical advantages, the biological effect of the same physical dose may be different for different types of radiation. This issue is discussed in more detail in the next section.

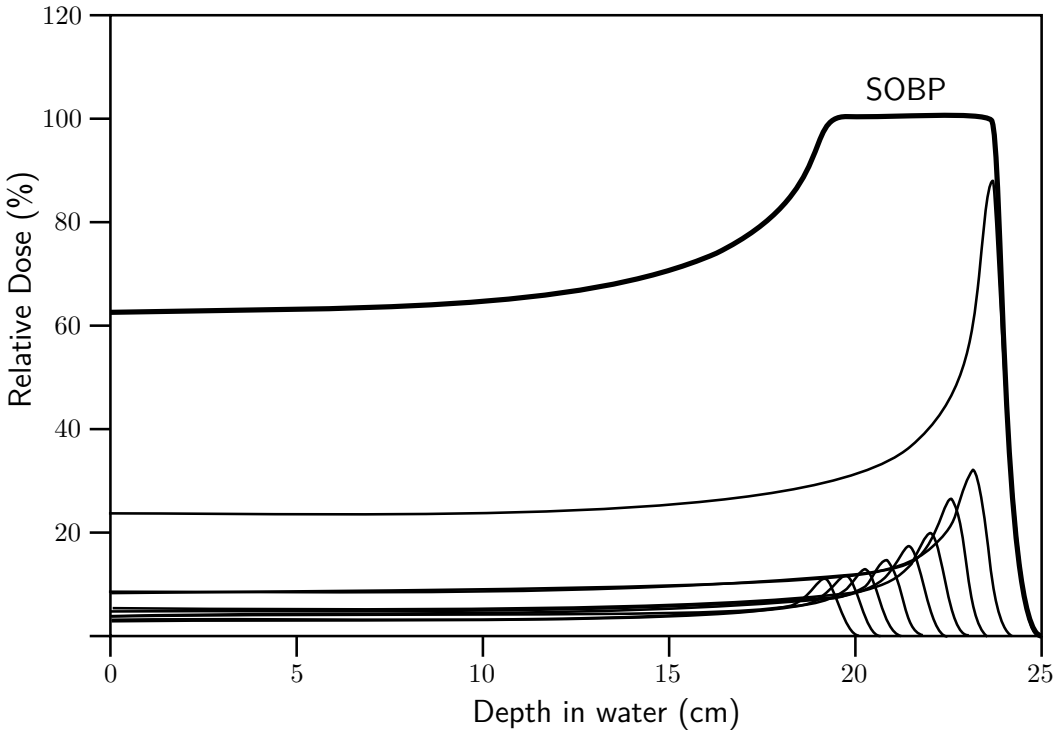

Figure 1.1: Construction of a spread-out Bragg peak (SOBP). Image adapted from [10].

1.2 Biological effect of ionizing radiation

Radiation therapy aims to introduce irreparable lesions to the DNA of cancer cells. These changes are supposed to prevent the cell from further proliferation or to trigger its apoptosis, i. e. its suicide program. Fitting the fraction of cells surviving irradiation of different levels of dose, in-vitro as well as in-vivo experiments show a relation between the absorbed dose, D, and the cell survival, S, that can be described by a linear-quadratic (LQ) exponential function [11]:

$$S = \exp\left[-\left(\alpha D + \beta D^2\right)\right] \tag{1.3}$$

Beyond its property of being just a reasonable fit to survival data, the ratio of the coefficients can be related to some radiological meaning: as α is the coefficient for the initial slope at small doses and β the coefficient for the curvature at larger doses, α/β describes the degree of response of the irradiated tissue. Large α/β ratios

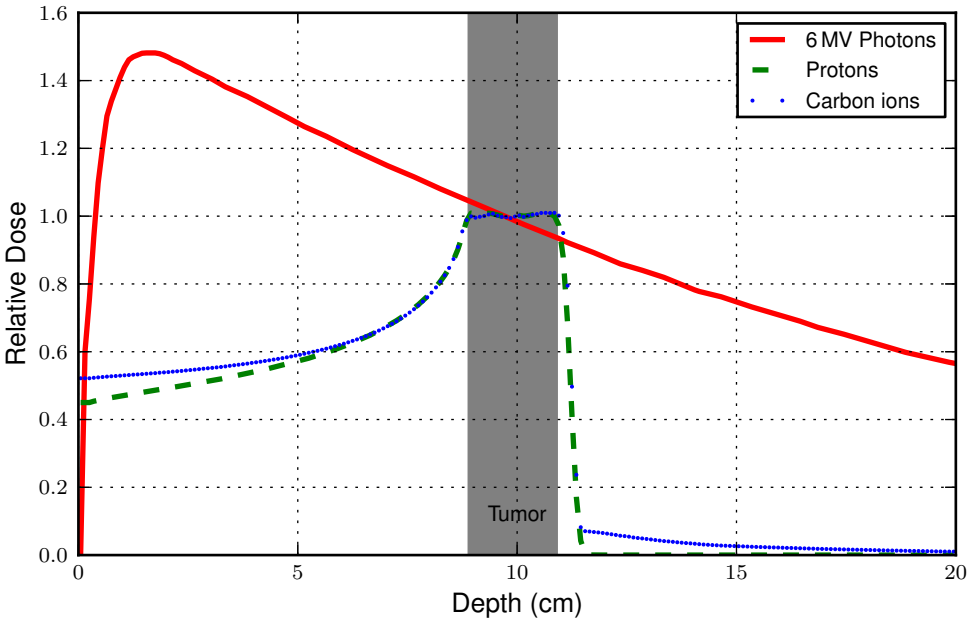

Figure 1.2: Depth-dose curves of 6 MV photons, a proton and a carbon ion spread-out Bragg peak (SOBP). Compared to the photon dose profile (red solid curve), the particle dose profiles (green dashed line for protons, blue dots for carbon ions) are inverted. The small amount of dose after the carbon ion peak is due to lighter particles generated in inelastic collisions which have a longer range. The biological effect of carbon ions is enhanced, particularly in the SOBP, and not shown here.

correspond to so-called "early" or "acute" reacting tissues, of which most tumors are part of, whereas small ratios correspond to late reacting tissues, which fortunately turns out to be the case for most healthy tissues. Consequently, a fractionation of the total dose, i. e. multiple irradiations with small doses during a longer time period, is often beneficial to save healthy tissue.

As mentioned, it has turned out that cells react differently to various types of irradiation, such that even if the physical dose D is the same, the survival S can be different. To compare the biological effect of various types of irradiation, the concept of relative biological effectiveness (RBE) has been introduced. It is the ratio of the physical dose of a reference radiation, generally ^{60}Co gamma rays, to a test

radiation achieving the same biological effect (e. g. survival fraction S):

$$RBE = \frac{D_{^{60}\mathrm{Co}}}{D_{\mathrm{x}}}\bigg|_{\text{iso-effect}} \tag{1.4}$$

Despite its rather simplistic definition as the above mentioned ratio, the RBE depends on many physical and biological parameters: dose, dose per treatment fraction, radiation quality (e. g. linear energy transfer, LET, definition in sec. 2.1.1), desired biological endpoint, cell type, the damage repair abilities of a cell, and many more. The dependence on LET will be described in more detail in sec. 2.1.2.

The planning of a cancer treatment aims to optimize for an optimal dose level in the target volume containing the tumor, and an as low as reasonably achievable level of dose in the surrounding healthy tissue. For treatment planning involving charged particles heavier than protons[2], this also includes the determination of the RBE throughout the irradiated volume, which is, as indicated above, not easily accessible. Therefore, models have been developed to estimate the RBE from physical, measureable, quantities. An implementation of the Local Effect Model (LEM) [13] is successfully used in determining the biologically effective dose in treatment planning at the Heidelberg Ion Beam Therapy Center (HIT). Japanese research groups use the Microdosimetric Kinetic Model (MKM) to calculate the RBE from quantities measured by microdosimetric equipment [14]. Both models assume that the biological effect depends solely on the energy deposited in small compartements of the cell, which is depending on the track structure of the radiation. The MKM is explained in more detail in chapter 3.

1.3 Present status and challenges in radiation therapy

The beneficial outcome of cancer therapy depends on the success of every link in the chain of steps involved, starting from tumor identification and localization (imaging), dose planning, patient positioning and the actual patient treatment.

The precision achievable with particle beam therapy can only be fully exploited when a precise knowledge of the target volume can be obtained. The imaging modality

[2]Even for protons some researchers argue that it may be necessary to take the varying RBE into account, especially if irradiation concepts like distal edge tracking are employed [12].

typically used for treatment planning is computed tomography (CT) because of the very good spatial resolution (1 mm and less) compared to other methods. However, the patient is exposed to additional dose as the modality uses X-rays. Furthermore, the soft tissue contrast is not high enough to resolve small tumor infiltrations into healthy tissue. Functional imaging like positron emission tomography (PET) and magnetic resonance imaging (MRI) can provide additional information about the tumor, like its metabolic activity or better information about the tissue composition. The aspects of imaging are discussed in more detail in [15].

One of the main challenges of using CT imaging in particle therapy is the uncertainty in converting the measured electron densities into water equivalent path lengths of charged particles needed to calculate their range. As a significant amount of dose is deposited in the Bragg peak at the end of the particle range, this very position has to be known as precisely as possible. The maximum error resulting from this density conversion is about 3 % [16]. To make sure that the whole tumor volume is covered with a high dose, the margins of the tumor volume are increased such that a too low range resulting from these uncertainties does not result in an underdosage. For X-ray therapy, this is not an issue because of the smooth decline in deposited energy along the depth (cf. fig. 1.2). To overcome the uncertainties involving X-ray CT conversion, research has been initiated to replace the X-rays by high-energy particles from the same facility that is also carrying out the treatment. The particles are energetic enough to exit the patient and a measurement of their residual energy allows a density reconstruction along the particle track [17, 18]. Several groups aim to image the Bragg peak position during the treatment by means of prompt-gamma or secondary charged-particle emission [19, 20, 21]. It was also shown that in the case of antiproton irradiation, the charged pions created in annihilation reactions can be used to reconstruct the Bragg peak position, in principle with an accuracy in the order of 1 mm [22]. The only method used successfully in a clinical routine environment is to take PET images after an irradiation fraction as the particle beam generates β^+ emitters (^{11}C, ^{15}O, ^{13}N, and ^{38}K) in the traversed tissue. In the case of carbon ions as beam particles, they become β^+ emitters (^{11}C, ^{10}C) themselves by inelastic nuclear scatterings along their trajectories. The areas with high PET activity can then be related to the range of the primary particles [23, 24]. Especially for protons, the activity pattern is however significantly different from the dose pattern, as activity is only generated when the protons have high enough energies to produce β^+ emitters in inelastic reactions. The situation is further complicated

if the imaging is performed after instead of during the treatment in order not to block the treatment facility, as the data acquisition time is in the order of tens of minutes. In this case, a large portion of the emitters has already decayed and the β^+ emitter distribution is distorted because of biological transport [25]. A detailed review about in-vivo proton range verification techniques is given in [26].

Also, the treatment planning is advancing due to new possibilities of functional imaging. The tumor is known not to consist of homogeneous tissue only, but shows different compartments that respond differently to radiation. For example, there can be subvolumes that are not well oxygenated because they are too far away from a blood vessel, the so-called hypoxic areas, and they express a very low radiosensitivity, i. e. a higher dose is needed to reach the same effect as for normoxic cells. This is because oxygen is an important component in the chain of free radical reactions created instantly after irradiation and, therefore, plays an important role in the biological effectiveness. Even though studies have shown that imaging of hypoxic areas is possible with special PET markers ([27] gives a good overview), the problem remains that the hypoxic regions can change over time. Nevertheless, tumor hypoxia and the need for additional dose in hypoxic volumes has been included in the GSI (Gesellschaft für Schwerionenforschung) research treatment planning application. Furthermore, it has been shown that hypoxic areas can be treated more effectively if the LET of the radiation in these areas is high [28, 29], as it will become more clear in chapter 2. In principle, it is also possible to optimize for a homogeneous dose and an arbitrary LET distribution within the tumor by means of a concept called LET painting [30, 31].

2 Linear Energy Transfer and its Optimization

This chapter deals with fundamental properties of the linear energy transfer (LET), its applications in radiation therapy planning and the different optimization techniques. In the scope of this work, the dose-averaged LET is optimized to cover the whole target volume with the maximum possible LET value while maintaining a flat dose profile. The technique can be extended to target specific subvolumes in the treatment volume identified as hypoxic, e. g. by functional PET imaging.

2.1 Basic properties of LET

2.1.1 Definition and averages of LET

The development of quantities describing the radiation quality started in the 1940s, when primary ionization densities were considered [32]. A more detailed overview of the history is disscussed in the corresponding ICRU Report [33]. The definition of LET is

$$LET_{\Delta} = \left(\frac{\mathrm{d}E}{\mathrm{d}l}\right)_{\Delta}. \tag{2.1}$$

It "is the quotient of $\mathrm{d}E$ by $\mathrm{d}l$, where $\mathrm{d}l$ is the distance traversed by the particle and $\mathrm{d}E$ is the mean energy-loss due to collisions with energy transfers less than some specified value Δ." [33] Thus, the LET is closely related to the electronic stopping power (cf. sec. 1.1). In fact, it is also called restricted stopping power, because of the cut-off value Δ. The reason to introduce such a threshold is to have a measure of

the energy deposited locally, in the vicinity of the primary particle track, as it is this local energy deposition that has a strong influence on the biological effect. Higher energy deposits may result in ionization electrons that have high enough energies to travel a certain distance, thus carrying away energy to more distant regions irrelevant for the local biological effect. Δ usually has the unit eV; the unrestricted LET, is commonly noted as LET_∞ (the maximum energy transfer, however, is not infinitely large, but given by kinematics) and is, identical to the negative stopping power $\frac{\mathrm{d}E}{\mathrm{d}x} = -SP$. Secondary particles with energies exceeding the cut-off value are treated as separate particles.

The LET with a certain threshold Δ is obtained by integrating the underlying formula yielding eq. 1.2 only to energy transfers up to Δ, instead of all possible energy transfers, which results in [33]

$$LET_\Delta = -\left(\frac{\mathrm{d}E}{\mathrm{d}x}\right)_\Delta = \frac{2\pi n z_{eff}^2}{m_e c^2 \beta^2} \cdot \left(\frac{e^2}{4\pi\varepsilon_0}\right)^2 \cdot \left[\ln\left(\frac{2m_e c^2 \beta^2 \Delta}{I^2(1-\beta^2)}\right) - \frac{(1-\beta^2)\Delta}{2m_e c^2} - \beta^2 - 2\frac{C}{Z} - \delta\right]. \quad (2.2)$$

To relate the LET to treatment scenarios, where many, possibly different, primary beam particles with different energies and angles impinge a target volume, and additionally, the number of secondary particles along a primary particle's track increases because of inelastic reactions, the distribution of LET is commonly expressed in two averages:

- Track- or fluence-averaged LET: integral form as defined in ICRU Report 16 [33]:

$$\overline{LET}_\mathrm{t} = \int_0^\infty t(LET)\, LET\, \mathrm{d}LET \quad (2.3)$$

  t(LET) is the track length distribution of particles with the linear energy transfer *LET*, it is weighted by the *LET* and integrated over all possible values of LET.

The discrete form is needed for computational purposes:

$$\overline{LET}_{\mathrm{t}} = \frac{\sum_z \sum_E LET\,(E;\,z)\,\Phi(E;\,z)}{\sum_z \sum_E \Phi(E;\,z)} \tag{2.4}$$

here, the LET of every particle species z and every occuring energy E is weighted by its fluence Φ, i. e. the number of particles $\mathrm{d}N$ incident on a sphere with the cross-sectional area $\mathrm{d}A$, having that particular species and energy, and the sum is normalized by the total fluence.

- Dose-averaged LET:

$$LET_{\mathrm{d}} = \int_0^\infty d(LET)\,LET\,\mathrm{d}LET \tag{2.5}$$

Compared to the track averaged LET, the weighting is done here by the dose instead of the fluence.
Its discrete form is:

$$LET_{\mathrm{d}} = \frac{\sum_z \sum_E LET^2(E;\,z)\,\Phi(E;\,z)}{\sum_z \sum_E LET(E;\,z)\,\Phi(E;\,z)} = \frac{\sum_z \sum_E LET(E;\,z)\,D(E;\,z)}{D_{\mathrm{total}}} \tag{2.6}$$

There is discussion in the scientific community about which of the averages is more related to a biological effect, some researchers even doubt the concept of LET in general, because it is a quantity averaged over energy deposits with a very wide range. Microdosimetry tries to overcome this problem and provides measurements of spectra of locally deposited energy in small volumes, considering this wide range of possible energy deposits. More details are discussed in chapter 3. However, it seems that there is a significant correlation between LET and the relative biolgical effectiveness (RBE), as will be discussed in the next section.

2.1.2 Influence of LET on RBE

As pointed out in sec. 1.2, the RBE is defined as the ratio of two doses of different radiation type resulting in identical biological effects and depends on many physical and biological quantities. Sørensen et al. [34] compared data reported on the RBE for different types of radiation. It turns out that in spite of the complexity of the

RBE concept, there is a significant correlation between the dose-averaged LET and the relative biological effectiveness, cf. fig. 2.1.[1]

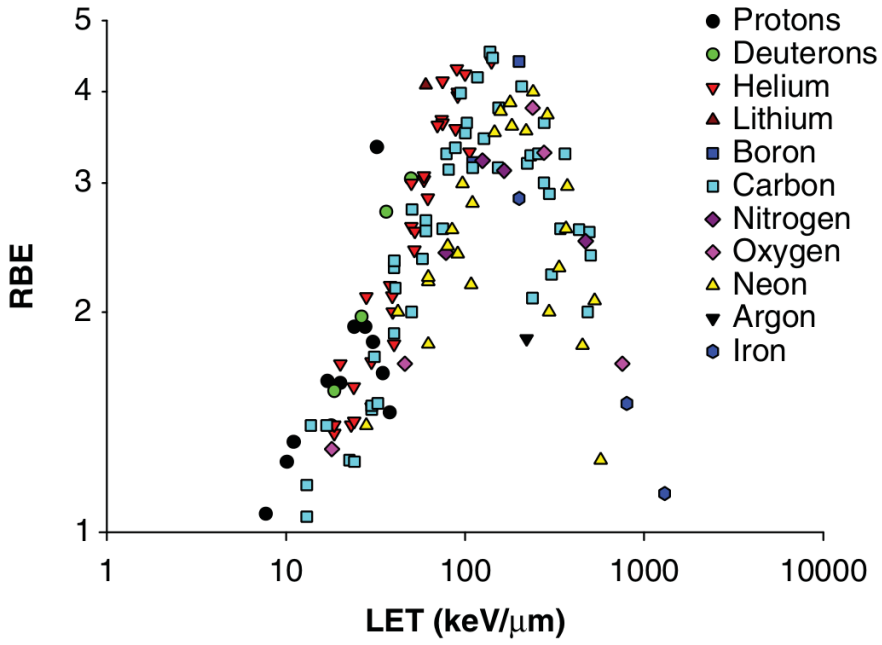

Figure 2.1: LET-RBE relation for V79 cells for different ions. Taken with permission from [34].

2.1.3 Influence of LET on OER

As pointed out in sec. 1.2, cells react differently to the same amount of dose but different radiation quality. In particular, there is a relation between the oxygenation of a cell and its radiosensitivity. If cells are provided with little or no oxygen, more dose is needed to kill them. The ratio of the dose needed to achieve a certain survival fraction S in a hypoxic situation and the dose needed at normal oxygenation is called oxygen enhancement ratio (OER):

$$OER = \frac{D_{\text{hypoxic}}}{D_{\text{normoxic}}}\bigg|_{\text{iso-effect}} . \tag{2.7}$$

[1] The authors of the cited publication do not explicitely name the average, but only refer to "LET". However, in the vast majority of the data sources they have collected, the dose-averaged LET was applied.

Wenzl et al. [35] review the LET-OER relationship measured by different experiments and conclude that there is a relation between LET and OER (fig. 2.2), and within the errorbars, the dependence on different particle types or cell lines is small. However, there is a significant difference in the LET-OER relationship reported for in-vitro and in-vivo situations, where the latter shows generally lower OER values.

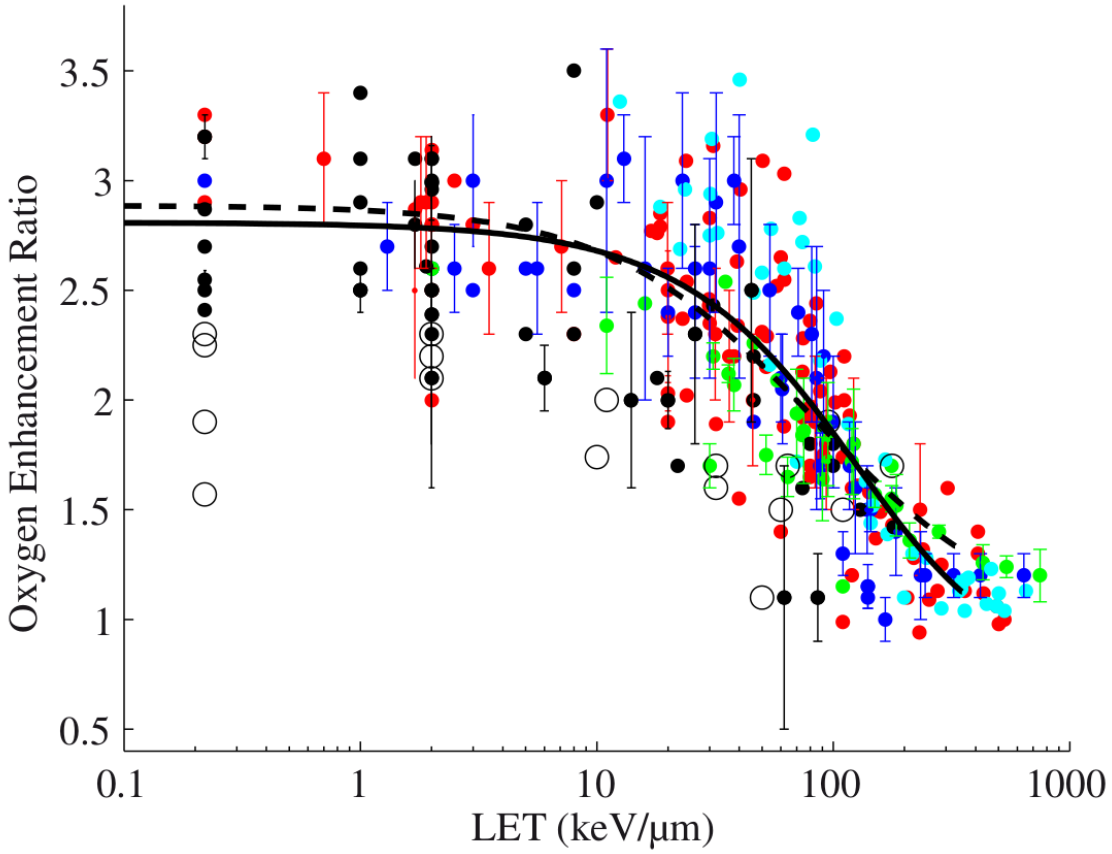

Figure 2.2: LET-OER relationship. Figure taken from [35]. Error bars from original publications, if provided. Different colors for different cell lines. *Open circles:* in-vivo data, *filled circles:* in-vitro data. *Dashed and solid line:* OER calculated from model presented in the publication.

2.1.4 Measurement of LET

Direct LET measurement devices do currently not exist. The main problem arises from the fact that a LET detector has to incorporate the cutoff-value Δ, in order to not include energetic secondary particles. Furthermore, the gradients of dose and LET distributions along the track of charged particles are high, especially at the

Bragg peak, which makes a high spatial resolution necessary. However, a promising approach is to use the effect of recombination, i. e. the "missing signal" due to signal quenching when using an ionization chamber where the active volume is a liquid in comparison with a signal from a regular air-filled ionization chamber. Together with data generated by Monte-Carlo simulations the LET can be assessed. For more information cf. [36].

Another approach is the usage of passive nuclear track detectors, such as the plastic-based track-etch detectors (CR-39) [37, 38, 39], or fluorescent nuclear track detectors (FNTD) [40], where the impact of the primary ions as well as the generated secondary particles can be made visible and the deposited energy assessed. However, compared to the technique previously described, a real-time measurement of the LET is not possible.

2.2 Dose and LET planning and optimization

2.2.1 Planning

Dose planning is one of the critical links in the chain of cancer treatment (cf. sec. 1.3). It is done after the tumor has been localized and delineated by a physician. Generally, the treatment plan consists of several volumes, making up the tumor volume itself and several extensions of that volume. Such volume extensions are described in a dedicated ICRU Report [41] and take all known uncertainties into account, e. g. the invisible infiltration of the tumor into the surrounding tissue, positioning uncertainties, and residual tumor motion. Furthermore, critical organs nearby that have low tolerance doses are included as constraints. It is a balancing act between assuring that the tumor is completely covered with the dose needed to kill it and to spare the healthy surrounding tissue from unnecessary dose. The optimal dose distribution is often obtained when multiple irradiations from different angles, the so-called fields, are optimized and irradiated. By this method, the tumor is always hit by radiation, but the unavoidable dose to the surrounding healthy tissue is spread over larger volumes. In *i*ntensity *m*odulated *r*adio*t*herapy (IMRT) using photons, usually 6–8 fields are applied, whereas due to the better intrinsic dose profile of particles, but also due to technical constraints (e. g. treatment time, gantries not universally available, etc.) the number of fields in particle therapy typically

is 1–3. Two opposing directions are often used to mitigate problems due to range uncertainties.

2.2.2 Optimization

Modern radiotherapy techniques like IMRT or *v*olumetric *m*odulated *a*rc *t*herapy (VMAT) for photon irradiation, or actively delivered particle therapy offer many degrees of freedom for performing the actual treatment. To achieve an optimal dose coverage across the tumor volume while minimizing the dose to the surrounding tissue and especially critical organs, computer software has been developed to optimize the technical parameters for each individual tumor. In some cases, the optimization is repeated if the tumor or the patient anatomy has changed in the course of the treatment. Different optimization techniques exist; usually they are based on the inverse planning method, i. e. finding the optimal parameters to achieve a predescribed dose distribution. In the particular case described in this work, the treatment is carried out by scanning a thin pencil beam of particles across the target volume. As a consequence, the typical combination of different beam positions, widths, energies, and fluences needed to cover a tumor volume with the desired dose accounts for many thousands of degrees of freedom. The underlying optimization routine minimizes the difference between the prescribed dose distribution and the dose distribution generated by a combination of fluences Φ of particles for each position $\mathbf{x}$, energy and beam width:

$$\begin{aligned} \chi^2 &= \sum w(\mathbf{x}) \left(D_{\text{prescribed}} - D(\mathbf{x})\right)^2 \\ \frac{\partial \chi^2}{\partial \Phi} &= 0 \end{aligned} \tag{2.8}$$

$w(\mathbf{x})$ is a weighting factor, the prescribed dose is a constant in eq. 2.8, but can in principle be an arbitrary dose distribution, e. g. a linear function as applied in sec. 2.3. For particles with varying RBE along their path, the biological dose is calculated in each iteration of the optimization process, such that the treatment plan can also be optimized for a homogeneous biological dose across the target volume. Furthermore, the quantity to minimize can be extended by constraints, e. g. including maximal tolerable doses to nearby organs at risk. A full overview of the algorithms and their implementation into the research treatment planning system *TRiP* (*tr*eatment

plann*i*ng for *p*articles) developed at GSI is given in [42, 43, 44]. Newer developments include the oxygenation status of the target and the dependence of hypoxia on LET into the planning, resulting in an inhomogeneous dose distribution to achieve a homogeneous biological effect [45]. Procedures like this are commonly called dose painting.

2.2.3 Dose and LET painting

As mentioned in sec. 2.2.2, the predescribed dose is constant in clinical practice because no further sub-divison of the tumor tissue is assumed. When deviating from the standard dose description, e. g. by applying the concept of dose painting to add additional dose to sub-volumes of the target volume, the total dose given to volumes outside the target volume is increased as well, because the additional, wanted, dose always comes along with inevitable dose due to the physical nature of dose deposition as described in sec. 1.1. In the case of hypoxia, where the OER depends on the dose-averaged LET of the radiation, one could also think of optimizing the dose-averaged LET to have sufficiently high values covering hypoxic areas, leaving the dose constant across the tumor volume, thus reducing the OER and finally the dose needed to achieve tumor control. However, the LET is closely connected to the particle's energy, in such that any given dose distribution has its own dose-averaged LET distribution, depending on the configuration of irradiation directions. As it will become clear in the following sections, for dose plans consisting of independently optimized fields, the dose averaged LET distribution is rather unfavorable, but there are ways to reshape the dose distribution to also change the dose-averaged LET distribution.

In addition, using different ions, however, makes it possible to decouple the LET distribution from the dose distribution to a larger extent. For example, a hypoxic subvolume of the tumor can be irradiated with heavy particles, such as oxygen ions, taking advantage of the z^2 dependence of the LET, while "filling up" the residual dose by lighter, lower-LET particles or even photons. The dose and LET painting concepts are explained in more detail in [46, 47, 48, 30, 31].

2.3 LET redistribution

The aspects of dose and LET optimization discussed in the previous chapters show the potential of advancements for future radiotherapy. However, the special treatment of subvolumes, e. g. hypoxic areas of the tumor is only justified if the imaging of the properties of these areas is possible in a stable, reproducible way. It seems, however, that apart from the search for an adequate marker for imaging, hypoxic areas are not always persistent in time, but can present themselves as acute hypoxia or chronic hypoxia. Acute hypoxia may change over the treatment process, such that a stable and reproducible imaging of these areas might turn out to be cumbersome, as the treatment process usually lasts several weeks. Furthermore, the clinical routine application of these developments require further experimental verification, clinical trials, and certification by legal authorities, such that the day at which large amounts of patients benefit from these developments lies in the rather distant future.

However, even with today's possibilities, a favourable dose-averaged LET can be achieved by reshaping the dose distributions of the single fields used in particle therapy. For a pristine Bragg peak, the LET maximum lies just after the rear fall-off of the dose. As a conventional flat-top spread-out Bragg peak is constructed by a weighted superposition of pristine Bragg peaks (cf. fig. 1.1) with the largest weight put on the peak at the rear part, also the dose-averaged LET shows a maximum right on or just behind the dose fall-off after the SOBP (cf. upper images in fig. 2.4 and fig. 2.5). This is unfavorable because of two reasons: first, the dose-averaged LET maximum is at the target volume's border, such that there is no beneficial effect on hypoxic areas that usually lie deep inside the tumor where the oxygen supply is diminished because of poor blood perfusion. Second, as there is a relation between dose-averaged LET and the RBE, the highly effective part of the radiation, not considering OER, is at the outer border of the target volume as well. Since the treated volume is already larger than the tumor volume to account for the uncertainties in the planning process, the high RBE component is simply wasted with high probability. Moreover, small errors in positioning or small changes in the patient's anatomy during the treatment process could make the highly effective dose area extend even further, possibly exceeding tolerance levels of healthy tissues nearby.

The natural conclusion is to change the weights and abandon the concept of overlaying two or more fields with a flat depth-dose distribution. For example, changing

the depth-dose distributions for a field towards a linearly decreasing dose in the peak region (dose ramp) still yields a flat depth-dose distribution if the two fields are overlayed from opposite directions (cf. fig. 2.3). Due to the changed weights of the pristine Bragg peaks, the dose-averaged LET distribution will also be changed.

The benefits are threefold: First, the dose-averaged LET can be redistributed across the tumor volume, as will be shown in the next chapter. Thus, the OER in hypoxic regions can be reduced. Second, the use of dose ramps results in superior dose plans when concave structures enclosing organs at risk are involved [49]. Furthermore, using overlapping opposing dose ramps makes the whole treatment plan more robust, as under- and overdosage areas resulting from imperfect overlay of the single fields with the target volume can be avoided. And last but not least, dose ramps are included in treatment planning software that is certified for clinical use already today, such that, in principle, LET maximization across the tumor volume is possible right now.

2.3.1 Methods

To demonstrate the beneficial distribution of the dose-averaged LET across the target volume using dose ramps, the clinical research tool *TRiP* version 1001c (cf. sec. 2.2.2), was applied. It is able to calculate the combination of energies, positions and widths of pencil particle beams needed to achieve a predescribed dose distribution.

The special method described here is the use of dose ramps to redistribute the dose-averaged LET. Different from dose painting, no additional dose is put into sub-regions of the target volume. By changing the parameters shown in fig. 2.3, it is possible to redistribute the dose-averaged LET to be constant throughout the target volume or to have a high value in a sub-volume. It is anticipated, however, that the achieved magnitude of the dose-averaged LET is not high enough to reduce the OER to values close to 1 using pure proton or carbon ion beams, when comparing the achieved 3 keV/µm for protons (fig. 2.4) or 75 keV/µm for carbon ions (fig. 2.5) with fig. 2.2. This becomes even worse with increasing size of the target volume. Nevertheless, even with the level achieved, the OER begins to change significantly towards lower values.

As the author is also involved in the Antiproton Cell Experiment (ACE), which aims at assessing the biological effectiveness of antiproton irradiation, a study involving

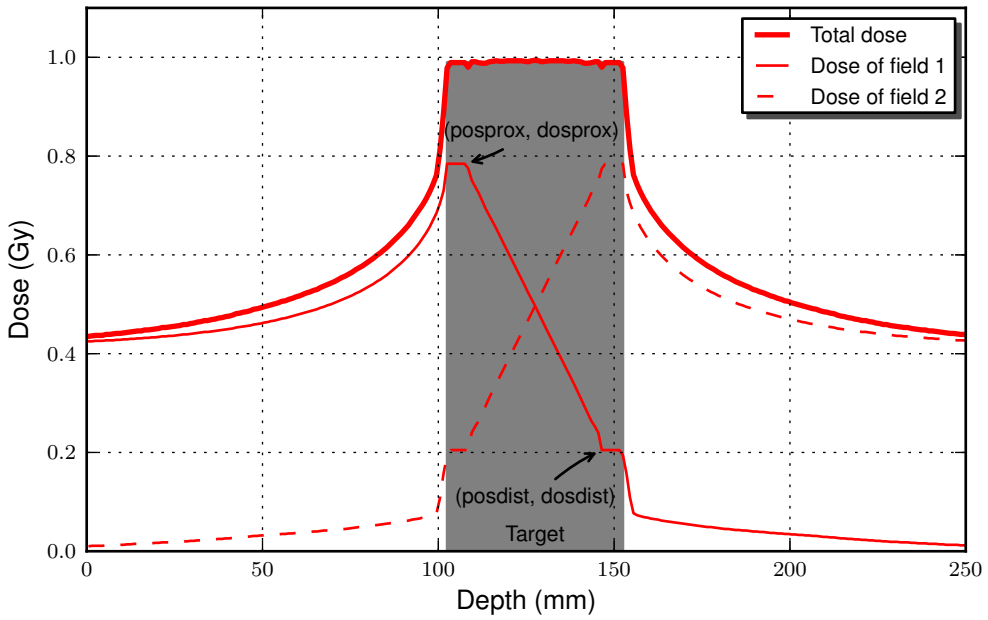

Figure 2.3: Dose ramp and its defining parameters. "posprox" and "posdist" mark the relative depth position in beam direction inside the target volume along which the dose ramp is located, "doseprox" and "dosedist" denote the dose levels before and after the ramp, respectively. In the graph shown, the parameters are represented by (0.2, 0.8) and (0.8, 0.2) for both fields.

antiprotons is also presented. As *TRiP* is not able to optimize for antiprotons because the handling of exotic particles like pions and kaons created in antiproton annihilation events is not implemented, a detour involving a full Monte-Carlo calculation using *FLUKA* version 2011.2b [50, 51] is done. Here, a library of depth-dose distributions of antiprotons with different energies was generated and the parameters to achieve flat SOBPs and dose ramps were manually optimized.

To demonstrate the method, a simple $20 \times 20 \times 50\,\mathrm{mm}^3$ target volume embedded in the center of a $255 \times 127 \times 255\,\mathrm{mm}^3$ water phantom was modeled. Treatment plans with two opposing fields using protons, carbon ions and antiprotons, respectively, were generated for the following scenarios:

1. Each field with flat SOBP making up half of the dose.
2. Each field consisting of a dose ramp decreasing from proximal to distal.

As the dose-averaged LET distribution reaches its largest values for carbon ions, a different redistribution is shown for this particle type to achieve even higher values.

The redistribution to gain a constant level of dose-averaged LET is shown for protons and antiprotons.

All plans are optimized for physical dose only to have a common basis of comparsion. Because the RBE of protons is set to 1.1 for clinical routine throughout the proton range, the physical and the biological dose is equal except for a constant factor. Moreover, the RBE assessment for antiprotons is still in progress at the time of writing this document.

2.3.2 Results

The dose and dose-averaged LET distributions calculated with the treatment planning tool *TRiP* for two opposing fields are compared for protons and carbon ions. For antiprotons, the distributions are calculated with the Monte-Carlo transport code *FLUKA*.

Protons

Because of the low charge of protons, their stopping power and, thus, their LET is low. The dose-ramp method allows for pulling the high dose-averaged LET region into the target volume, but regarding the OER (cf. fig. 2.2), no significant improvement is expected. Moreover, because of the lacking LET advantage, the dose-ramp case looks inferior to the standard case in this scenario because of the higher dose outside the target.

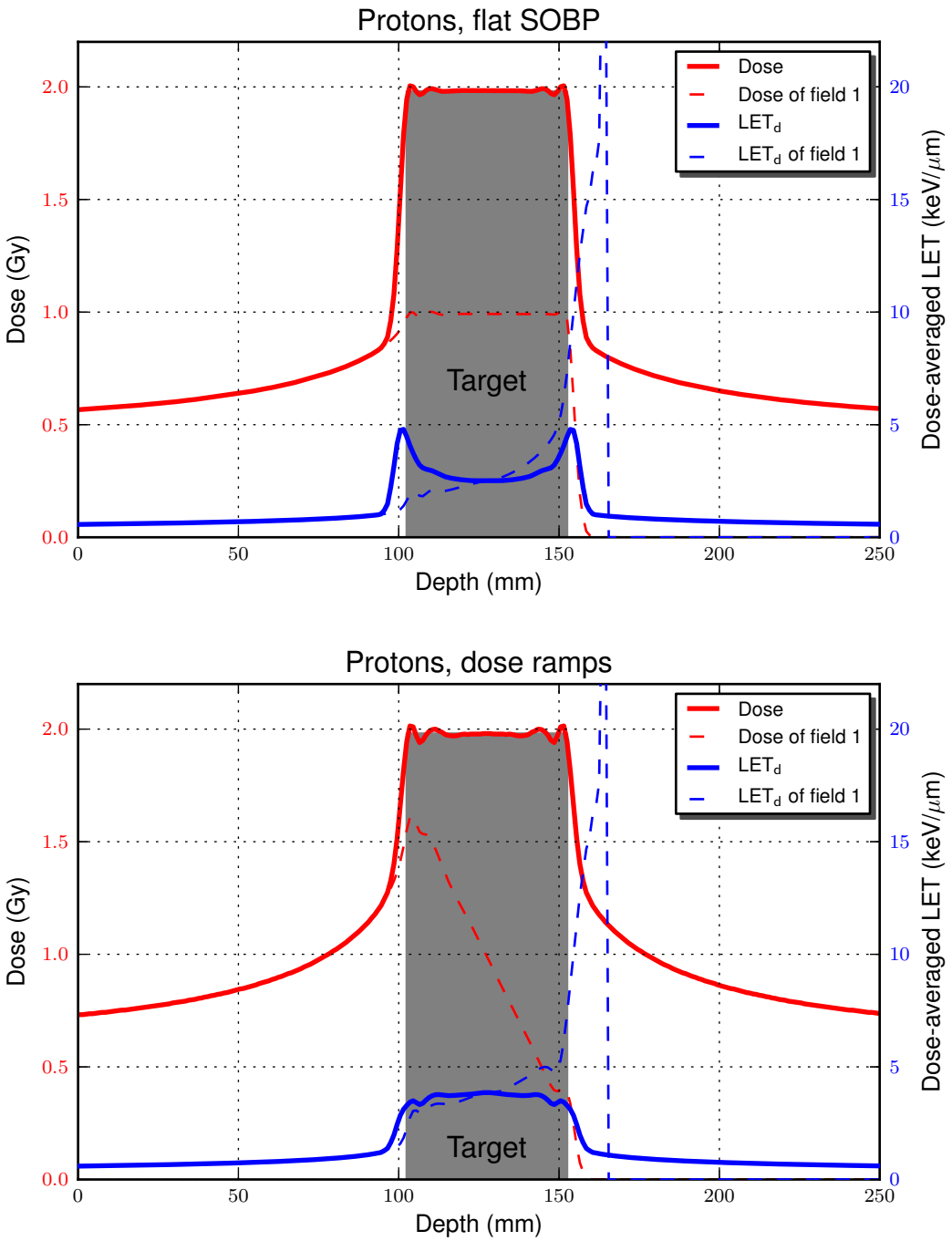

Figure 2.4: Dose (red) and dose-averaged LET (blue) for protons. *Top:* flat SOBP, *Bottom:* dose ramp. For the sake of clearness, the second, opposing, field is not drawn. The LET$_d$ peak of field 1 is suppressed in the total LET$_d$ distribution because it is weighted with the very low dose of field 1 at the peak position. Within the target, the average value and the standard deviation from the average of LET$_d$ is 2.90 ± 0.51 keV/µm for the flat SOBP and 3.67 ± 0.17 keV/µm, i. e., higher and more homogeneous for the dose ramp, respectively.

Carbon ions

Because of the z^2 dependence of the stopping power, also the LET is increased significantly. It is, however, not exactly 6^2=36 times higher as for protons as also lighter fragments with lower LET contribute to the dose-averaged LET.

In the standard SOBP case, the dose-averaged LET has a rather low value (about 50 keV/µm) in the center, but peaks just at the borders of the target region. Generally, the hypoxic areas are inside the tumor and not on its edge as the normal tissue around has good blood perfusion, such that the high $\mathrm{LET_d}$ is wasted at that position. For the ramp case, the dose-averaged LET is distributed nearly equally across the whole volume and reaches a reasonable high value of about 75 keV/µm. This is still not high enough for a decrease of the OER to values close to 1, but compared to the standard SOBP, there is already a significant change.

As announced above, the redistribution towards achieving high values of dose-averaged LET are demonstrated here as well. In the example illustrated in fig. 2.6, the dose-averaged LET was redistributed to peak at about 118 mm depth with a width of about 10 mm. The dose ramp parameters (cf. fig. 2.3) chosen are (posprox= 0.2, dosprox=0.8), (posdist=0.4, dosdist=0.2) for field 1 and (0.6, 0.8), (0.8, 0.2) for the opposing field 2, respectively. This yields dose-averaged LET values between 100 and 110 keV/µm within 1 cm around the peak, such that a significant OER-effect can be expected in this area.

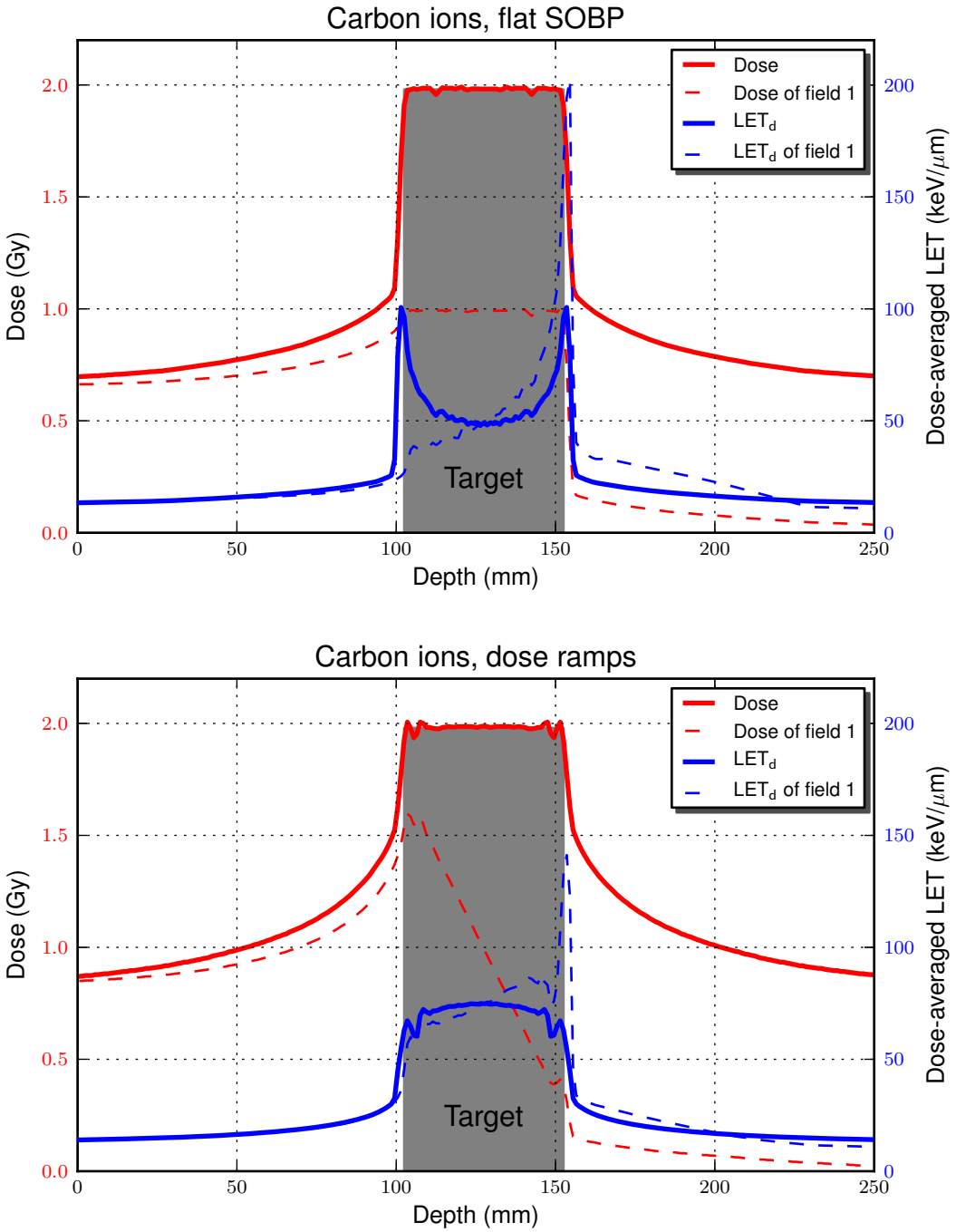

Figure 2.5: Dose (red) and dose-averaged LET (blue) for carbon ions. *Top:* flat SOBP. *Bottom:* dose ramp. Within the target, the average value and the standard deviation from the average of LET_d is $57 \pm 11\,\mathrm{keV/\mu m}$ for the flat SOBP and $71.2 \pm 4.3\,\mathrm{keV/\mu m}$, i. e., higher and more homogeneous for the dose ramp, respectively.

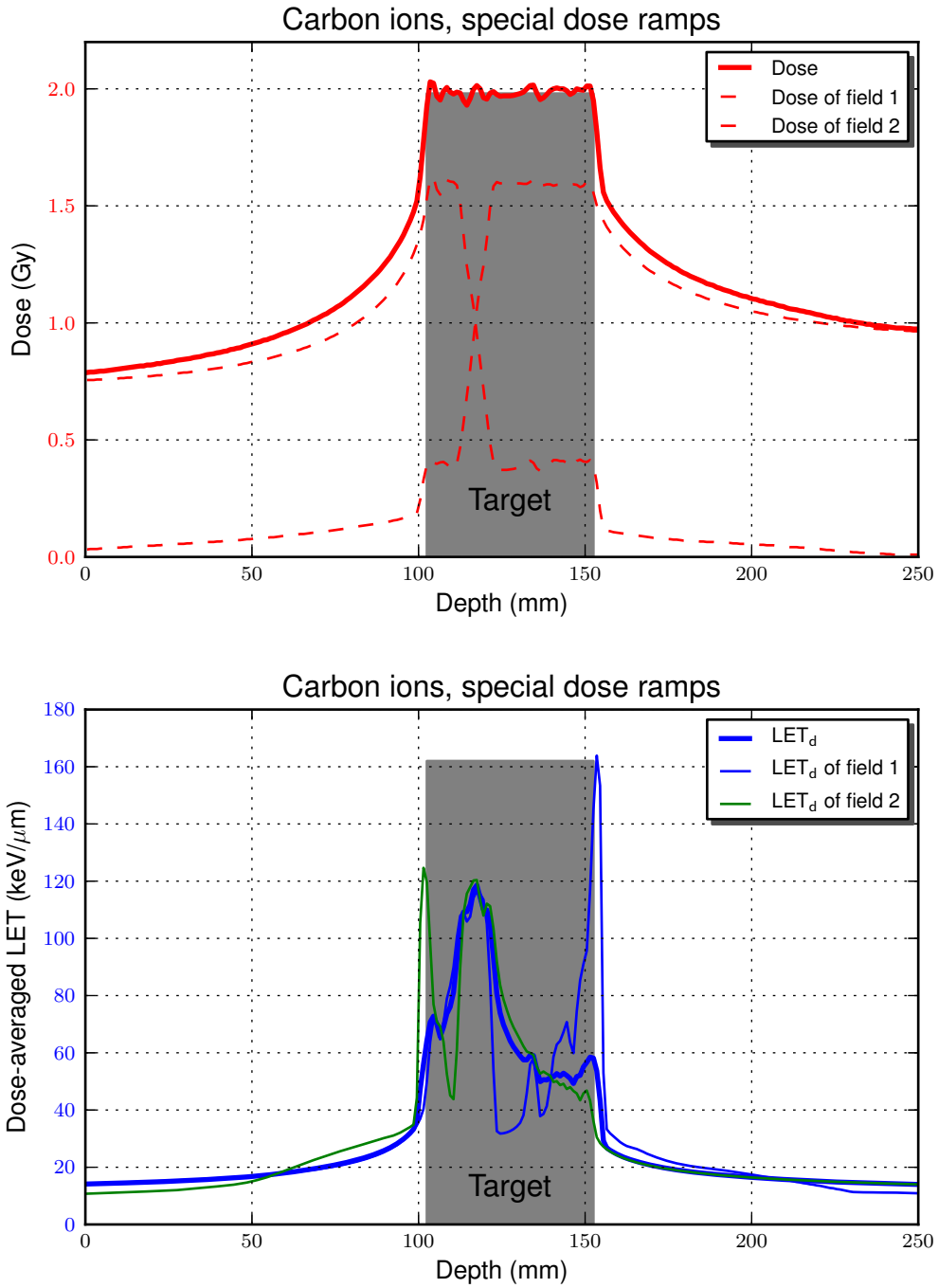

Figure 2.6: Dose and dose-averaged LET redistribution to peak at about 118 mm depth with a width of about 1.5 cm. *Top:* construction of the dose distribution. *Bottom:* dose-averaged LET distribution. Within the target, the average value and the standard deviation from the average of LET$_d$ is 71 ± 22 keV/µm.

Antiprotons

The comparison of proton and antiproton data shows two principal differences: because antiprotons annihilate at rest, the dose yielded in the Bragg peak is higher by a factor of 2 compared to protons. This makes the entrance dose for antiprotons significantly lower as less particles are needed for the same peak dose. However, charged secondary particles generated in annihilation reactions, especially pions, have long ranges and account for the smoother distal fall-off and an additional, but low, ambient dose throughout the volume. The dose-averaged LET for antiprotons is significantly higher than for protons, especially in the peak region the values are approximately twice as high, however, for the same dose ramp parameters as in the proton case, the dose-averaged LET distribution is not as homogeneous in the target, but shows a plateau in its center. The elevated values outside the target region are attributed to in-flight annihilation events. Compared to the values of carbon ions, they are still too low to significantly reduce the OER.

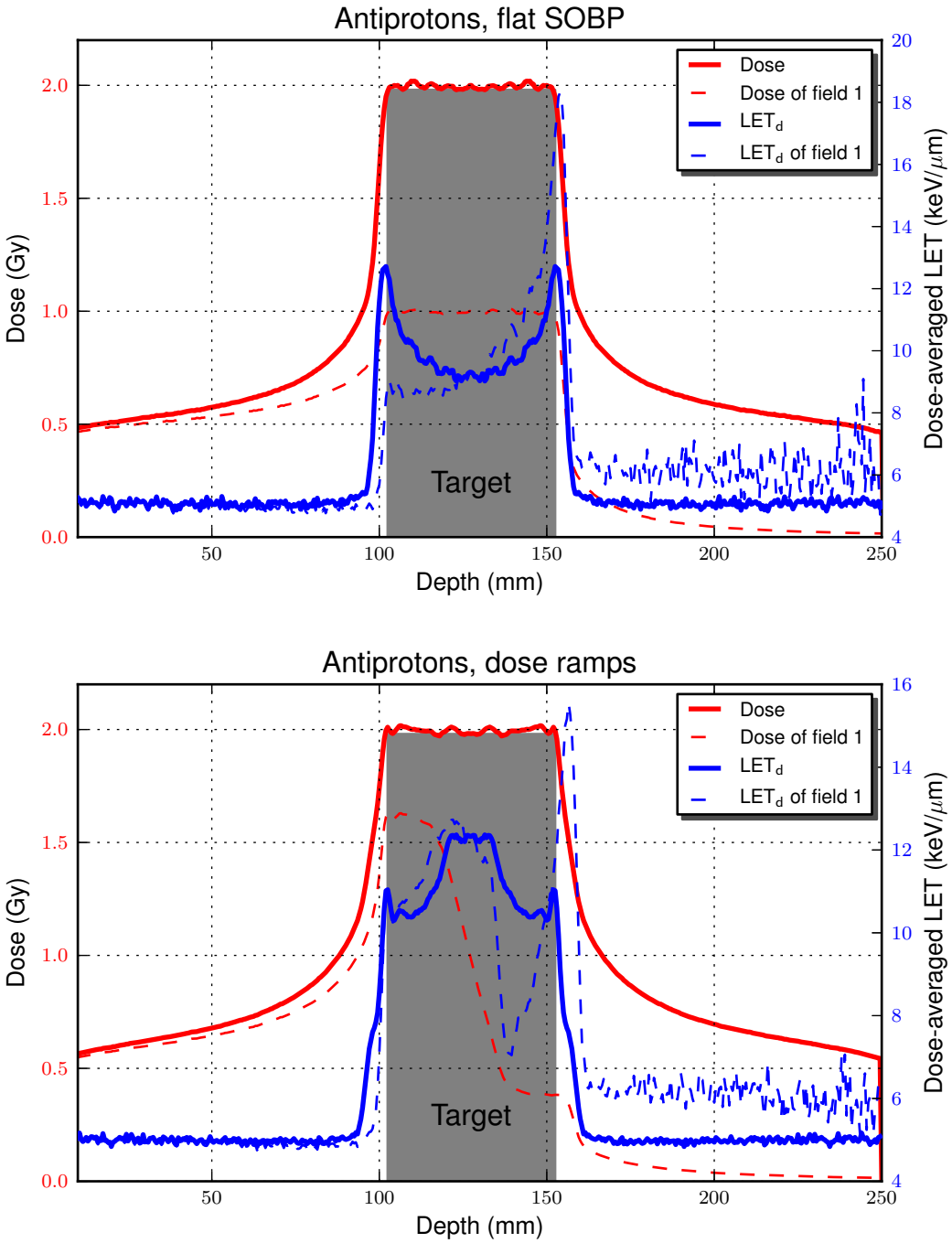

Figure 2.7: Dose (red) and dose-averaged LET (blue) for antiprotons. *Top:* flat SOBP. *Bottom:* dose ramp. The dose-averaged LET is not constant in this case, due to the different distribution of LET$_d$ for each individual field. Consequently, to achieve a flat combined LET$_d$, other shapes than ramps are needed. Within the target, the average value and the standard deviation from the average of LET$_d$ is 9.97 ± 0.91 keV/µm for the flat SOBP and 11.14 ± 0.84 keV/µm for the dose ramp, respectively.

2.3.3 Discussion

Using dose ramps offers an easy way of redistributing the dose-averaged LET. Due to the z^2 dependence of the stopping power, best results are obtained with carbon ions, where the achieved values correspond to a decrease of the OER from 2.8 to about 1.8–2.0 (cf. fig. 2.2). Further improvement can be reached for heavier particles like oxygen, which are already available at HIT for experimental purposes. However, heavier particles have an elevated biological effectiveness already in the entrance region, making their exclusive use unfavorable. High enough values reducing the OER close to one with no deterioation of the overall biological dose distribution are only reached when more sophisticated methods are applied, like the dose and LET painting method mentioned earlier in sec. 2.2.3, where only the hypoxic areas are irradiated with heavy particles, while the residual target is treated with low-LET radiation. Compared to dose and LET painting, the method presented here could in principle already be applied in clinical cases today. Furthermore, more complicated patterns can be realized if the number of fields is increased. In this case, dose ramps would need to be replaced by some more sophisticated shapes.

Preliminary results of the Antiproton Cell Experiment (ACE) state that the biologically effective dose ratio (BEDR) of antiprotons compared to protons is 3.75 [52]. Considering the relatively low LET of antiprotons, the enhanced biological effect of antiprotons seems not to be a direct consequence of their dose-averaged LET, if the relation LET-RBE in fig. 2.1 is applied. In fact, the damage on cellular components like the DNA caused by a single particle impact has been observed by the collaboration to be more pronounced as for carbon ions in the SOBP [53]. This could possibly be the result of many single damages clustered in the close vicinity of the annihilation point.

3 Microdosimetry: do neutrons make the difference?

This chapter deals with microdosimetric measurements. Here, the stochastic nature of ionizing radiation in microscopic volumes can be revealed, which allows to provide statements about the radiation quality and its biological effectiveness. Microdosimetry evolved from the need to measure energy depositions by different ionizing radiation types in tissue within distances of 0.1 µm to 1 µm, the length scale of chromosomes. This is due to the fact that changes in the DNA are the most prominent precursors of cell mutations and death, and the fact that different radiation types showed significant differences in their effectiveness in causing these changes [54].

The main objective of this work was to compare spectra taken in two different particle therapy scenarios: one represents an actively delivered ion beam which is scanned across the target volume by magnetic deflection and change of the beam's energy at the accelerator level. Consequently, only diagnostic devices are in the beam path, i. e. the beam is "clean" and consists almost purely of the primary ions when it impinges the patient. The other scenario resembles a passive system where the beam has to traverse different materials that change its energy and shape to cover the tumor. Here, the beam consists of a variety of secondary particles produced in inelastic events in these materials, possibly containing a significant amount of neutrons which have an adverse biological effectiveness distribution and also might be a cause for therapy-induced secondary cancers [55].

The question is if the setup used in this work is sensitive enough to measure changes between these two scenarios, which could in principle qualify it to also detect sudden changes in the beam composition due to accidental introduction of unwanted material in the beam path.

3.1 Basics of microdosimetry

3.1.1 Conceptional aspects

Apart from the magnitude of the dose, the spatial pattern and characteristics of ionization events of a radiation type has a considerable influence on its biological effect, as illustrated in fig. 3.1. The concept of linear energy transfer (LET) already aims towards relating this pattern to an effect (cf. sec. 2.1.2), but it neglects the stochastic nature of ionization events. Microdosimetry aims to provide a more fundamental and general insight. It is defined as "the systematic study and quantification of the spatial and temporal distribution of absorbed energy in irradiated matter" [56]. Microdosimetry can be further sub-divided into regional microdosimetry, where energy absorbed from ionizing radiation is evaluated at volumes of certain extensions, called *sites*, not regarding the microscopic distribution of energy depositions within the site. The site concept naturally determines the energy deposited locally by means of a limited volume, i. e. a geometric cut-off, such that energetic secondary particles can escape it and deposit their energy elsewhere, while on the contrary, the LET concept refers to locally deposited energy by introducing a energy cut-off value Δ as described in sec. 2.1.1.

Most experiments are carried out in the branch of regional microdosimetry. The other, more theoretical, branch is called structural microdosimetry, where the microscopic pattern of energy absorption, the so-called inchoate distribution, is used to estimate the effect of ionizing radiation by combining the inchoate distribution with the pattern of sensitive structures, also considering migration of energy from the positions where it has been deposited to the structures. This work will exclusively be concerned with the experimental branch. The basic quantities presented here, as well as a more extensive introduction into the field can be found in [56].

The most important basic quantity of microdosimetry is the *energy deposit*, which is the energy ε_i absorbed at a *transfer point*, e. g. an atom:

$$\varepsilon_i = E_{in} - E_{out} + Q \tag{3.1}$$

E_{in} is the energy of the incoming ionizing particle, not including its rest energy; E_{out} is the sum of energies of all particles leaving the transfer point, again not

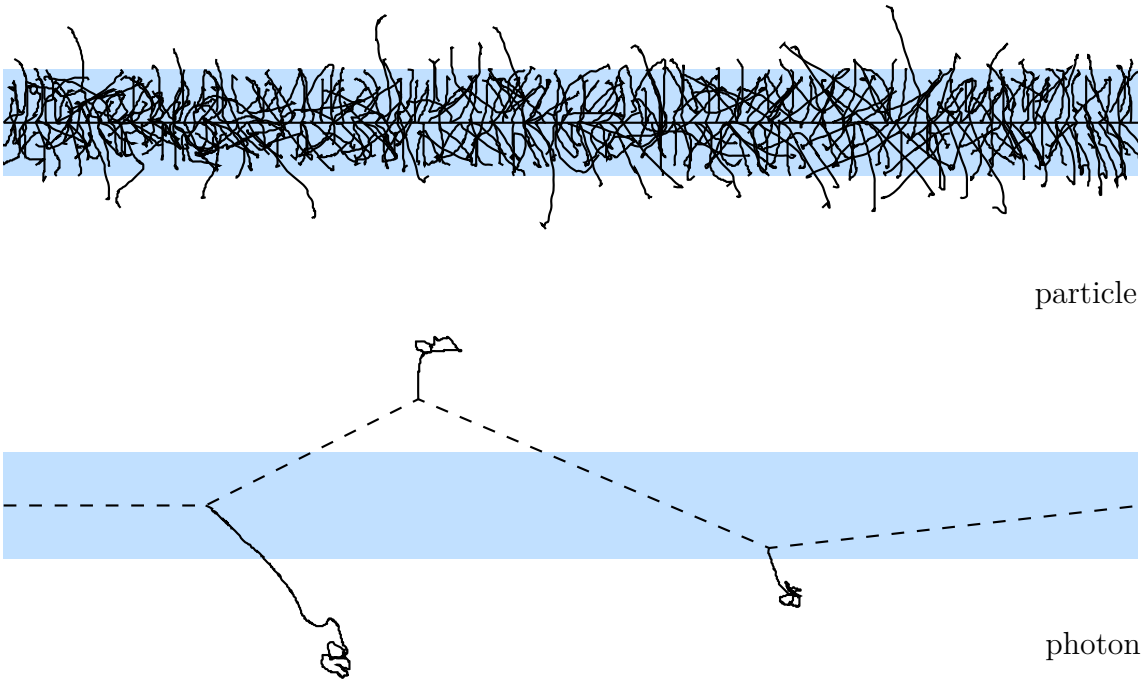

Figure 3.1: Illustration of different ionization patterns. *Top:* a particle, e. g. a carbon ion, causes many ionizations along its track, with low energies and ranges of the ejected electrons. The energy is densely deposited around the track. *Bottom:* a photon interacts with the surrounding matter in a more sparse way due to the lower interaction cross section. The ejected electrons, created by photoabsorption, compton scattering or pair production, have high energies and ranges. Consequently, little energy is deposited in the surroundings of the photon's path.

including rest energies. Q is energy either released ($Q > 0$) or absorbed ($Q < 0$) at the transfer point by changes of the rest mass of particles involved, e. g. due to nuclear reactions or pair production. The transfer point is the position where the interaction has happened, not regarding quantum mechanical uncertainty with respect to its location. The process is illustrated in fig. 3.2.

The term "ionizing" is generalized to any form of energy transfer in a single interaction, including non-ionizing events. This is owed to the fact that the biological effect not necessarily is a consequence of ionization, but also of changes of conformation of molecules, e. g. due to excitation. This generalization is accounted for by introducing a classification of transfer points, in such that *significant transfer points* mark *significant energy deposits*, i. e. deposits above a minimum threshold $\varepsilon_i \geq \omega$ to be able to cause the change under consideration. The average number N_R of *relevant transfer points*, where the change under consideration has actually occured,

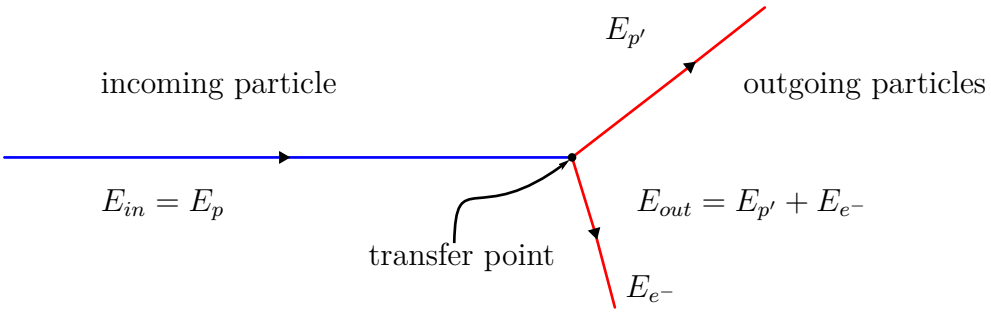

Figure 3.2: Illustration of an energy deposit

can therefore be expressed as:

$$N_R = \int_{\omega}^{\varepsilon_{i,max}} N(\varepsilon_i) p(\varepsilon_i) \mathrm{d}\varepsilon_i, \tag{3.2}$$

with $\varepsilon_{i,max}$ is the maximum energy deposit, $N(\varepsilon_i)\mathrm{d}\varepsilon_i$ the number of transfer points in the interval $[\varepsilon_i,\ \varepsilon_i + \mathrm{d}\varepsilon_i]$, and $p(\varepsilon_i)$ the probability that the change is due to the energy deposit ε_i.

The number of relevant transfer points gives an estimate for the probability of radiation effects to occur. However, also the geometrical distribution of the transfer points becomes important, if the effect is caused by more than one change. This is especially important for statistically correlated relevant transfer points that are created along a track of a charged particle.

Microdosimetry uses the concept of the *(energy deposition) event,* which is the production of statistically correlated transfer points, to characterize this correlation. In regional microdosimetry, the energy deposited in one or more events, $\varepsilon = \sum_i \varepsilon_i$, is the sum of all energy deposits in a delimited volume, called the *site*, cf. fig. 3.3. It is common to use ε_1 to refer to events that are caused by a single particle and its secondary particles only.

Because the underlying physical processes are stochastic, ε also is a stochastic quantity.

It is furthermore important to distinguish the energy expended by the incoming particle at a transfer point from the energy absorbed, as secondary particles produced at the transfer point may have high enough energies to transport a significant fraction of the expended energy away, outside the site. This is similar to the cut-off

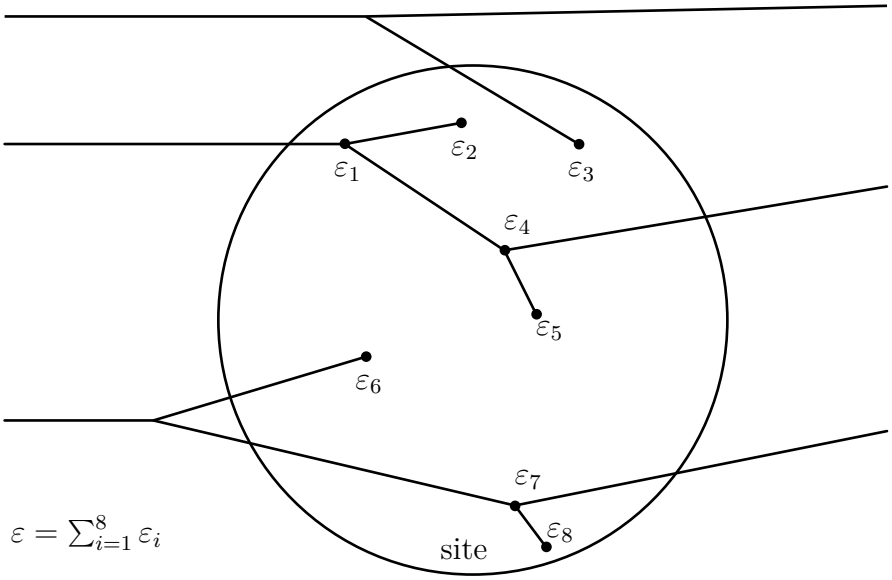

Figure 3.3: Illustration of events in a site. If all of the three particles coming from the left originated from the same primary particle, the situation would be termed "single event".

value Δ which was introduced in the LET concept in sec. 2.1.1, which also limits the energy considered to transfers below Δ.

The stochatic analogon to the physical dose is the *specific energy* z, which is defined as:

$$z = \frac{\varepsilon}{\rho \cdot V} = \frac{\varepsilon}{m} \tag{3.3}$$

It is the energy ε absorbed in one or more than one statistically independent events in a site that has the density ρ and the volume V, i. e. the mass m. Consequently, z has a probability density distribution, $f(z)$, which is also called frequency distribution, and whose variance increases, if the volume is decreased. For very small volumes, z can even be equal to zero, because the volume does not contain any transfer point. Thus, statements on z or $f(z)$ must include information about the volume V. The specific energy has the same unit as the physical dose, $1\,\mathrm{Gy} = 1\,\mathrm{J\,kg^{-1}}$.

The *lineal energy* y is a quantity similar to the linear energy transfer:

$$y = \frac{\varepsilon_1}{\bar{l}} \tag{3.4}$$

It is defined as the energy absorbed in a single event, ε_1, along the site's mean chord length $\bar{l}$, which is the average length of randomly oriented chords. In convex volumes, Cauchy's theorem yields for the mean chord length $\bar{l} = \frac{4V}{S}$, where V is the volume and S the surface of the volume, which gives $\bar{l} = \frac{2}{3}\,d$ for spheres, with d being the diameter of the sphere. The unit is $\mathrm{J\,m^{-1}}$, but usually it is expressed in $\mathrm{keV\,\mu m^{-1}}$.

For the following definitions of averages of the specific and lineal energies, it is convenient to regard ε continuous, even though it is discrete because it is the finite sum of energy deposits with well-defined, discrete, values.

The frequency average is the first momentum of the frequency distributions, the dose average is the second momentum of the distributions divided by the first:

$$y_F = \int_0^\infty y\, f(y)\,\mathrm{d}y; \qquad y_D = \frac{1}{y_F}\int_0^\infty y^2\, f(y)\,\mathrm{d}y \tag{3.5}$$

$$z_F = \int_0^\infty z\, f_1(z)\,\mathrm{d}z; \qquad z_D = \frac{1}{z_F}\int_0^\infty z^2\, f_1(z)\,\mathrm{d}z \tag{3.6}$$

$f_1(z)$ represents the propability density distribution of z where a single event has happened, making it independent of the total dose. Consequently, $f_1(z)$ is not defined at $z = 0$. While z_F can be identified with the physical dose, there is no direct relation between y_F and the linear energy transfer as, for a single event, y and z are only different by a numerical factor in the case of a single event:

$$z = \frac{\varepsilon_1}{m} = \frac{y \cdot \frac{4V}{S}}{m} = \frac{4y}{\rho S} \tag{3.7}$$

Measurements are typically represented as function of y.

3.1.2 Practical aspects

Measuring something small with something big

The prinicpal measurement device is the tissue-equivalent proportional counter which will be described in more detail in sec. 3.2.1. It is able to measure energy deposition events in volumes with extensions in the range of micrometers, even though its physical size is larger, typically in the order of a few centimeters. This is possible due to Fano's theorem stating that "in a medium of given composition exposed to a uniform fluence of primary radiation, the fluence of secondary radiation is also uniform and independent of the density of the medium as well as the density variations from point to point" [57]. This allows to replace the microscopic volume with a certain density by a larger gas volume of equivalent effective density (cf. fig. 3.4), if the condition expressed in eq. 3.8 is fulfilled.

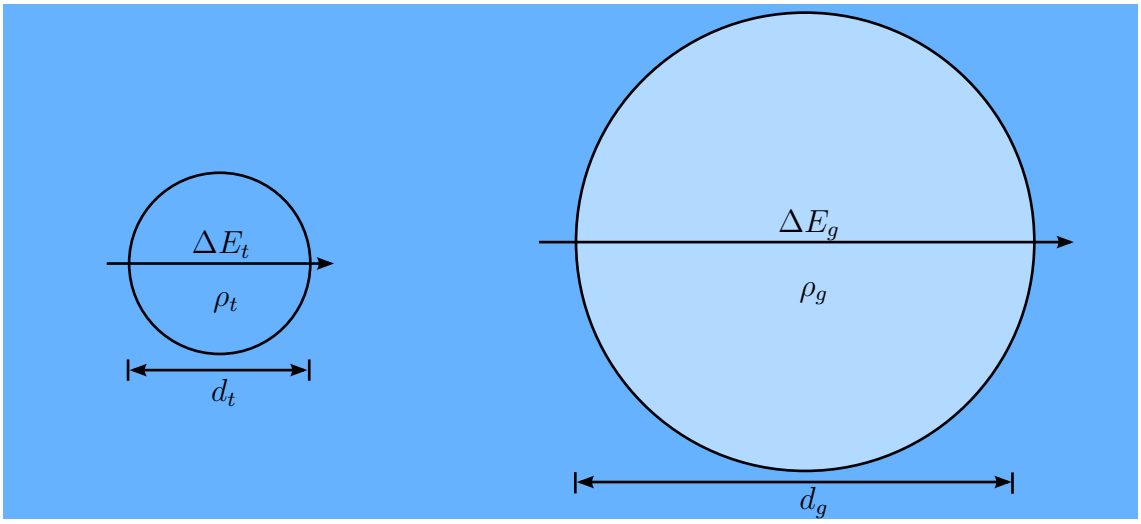

Figure 3.4: Fano's theorem (Eq. eq. 3.8, eq. 3.9) allows for replacing the microscopic tissue site (diameter d_t, density ρ_t) by a larger site of lower density (d_g and ρ_g, respectively), such that the energy loss of a particle ΔE_t in the tissue volume is the same as ΔE_g in the larger equivalent volume.

$$\Delta E_t = \left(\frac{1}{\rho}\frac{\mathrm{d}E}{\mathrm{d}x}\right)_t \rho_t d_t = \left(\frac{1}{\rho}\frac{\mathrm{d}E}{\mathrm{d}x}\right)_g \rho_g d_g = \Delta E_g \tag{3.8}$$

$$\rho_t d_t = \rho_g d_g \tag{3.9}$$

The term in brackets is the mass stopping power, the indices t and g represent tissue and the gas, respectively. $d_{t,g}$ are the diameters of the microscopic and the gas volume, and $\rho_{t,g}$ their densities, respectively. In eq. 3.9, the assumption was made that the stopping powers of tissue and the gas inside the detector are identical, which is only true if the atomic composition of the wall of the detector and the gas inside is the same as for the tissue, which is met as good as possible (see tab. 3.1), but not exactly. To simulate a certain volume size, the gas density is varied by changing its pressure p_g which can be, assuming ideal gas characteristics, calculated by

$$p_g = p_0 \cdot \frac{d_t}{d_g} \frac{\rho_t}{\rho_0}, \tag{3.10}$$

where the subscript 0 corresponds to the normal conditions of the gas.

Wall effects

The concept of a microdosimetric measurement is based on replacing a microscopically small volume by a larger volume with a lower density. In typical detectors, the low density volume is confined by a wall which has a higher density, which causes distortions of the signals. They are called wall effects and result in a higher energy deposited in the detector as additional particle tracks traverse the detector. As a consequence, to avoid these effects, wall-less counters have been designed, where the solid wall is replaced by a thin mesh of tissue-equivalent material [58].

Three types of wall effects are distinguished and illustrated in fig. 3.5 and fig. 3.6. In each of the figures, the left picture represents the microscopic site, without any density change at its outer border. The middle picture shows the situation if the microscopic tissue volume is replaced by a thin gas, including the size scaling to be equivalent to the dense scenario, which is resembled by wall-less counters. The right picture demonstrates the scenario with the detector consisting of a dense wall and a thin gas.

The delta-ray effect in fig. 3.5 refers to a situation where a primary particle generates a delta-ray before entering the site. In the case of uniform density of the site and its surroundings, as it is the case in tissues and in wall-less counters, either the primary particle or the delta-ray enters the site. However, in the case of walled counters, it is possible that, due to the dense wall, both the primary particle and its

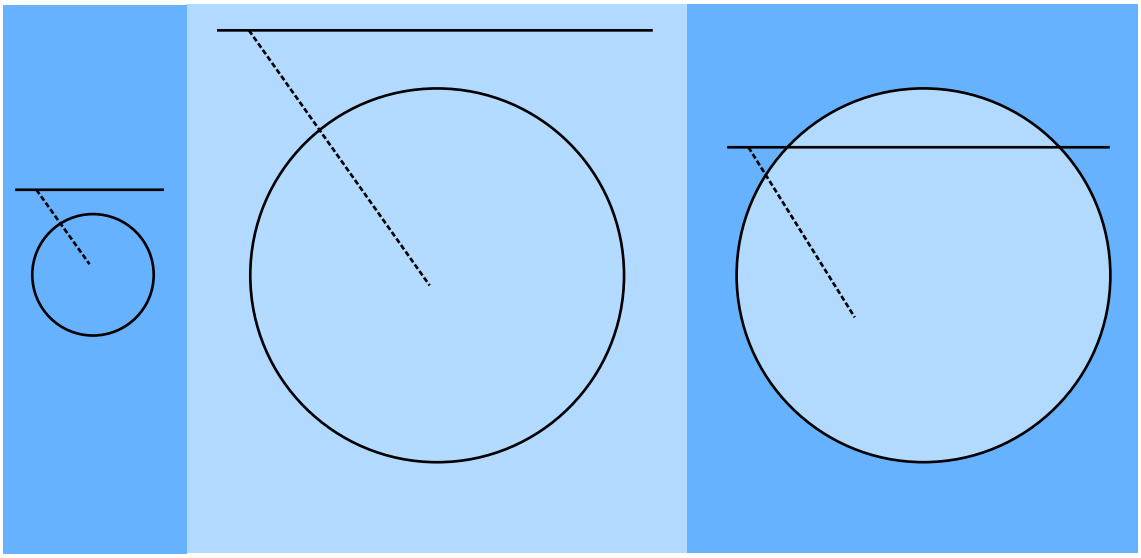

Figure 3.5: The delta-ray effect. A primary particle generates a delta-ray before approaching the site. *Left and center:* only the delta-ray enters the site because the density of the surrounding is the same. *Right:* situation in walled counter, where the surrounding of the site is denser.

delta-ray enter the site. The effect is most prominent for heavy charged particles, but the energy contribution of the delta-ray is low compared to the one of the heavy particle, such that the distortion of the energy-weighted y_D is lower that that of y_F. However, both averages are overestimated substantially if the secondary particle is not a delta-ray, but a heavy charged particle resulting from an inelastic scattering reaction of the primary particle, which is called V-effect.

The re-entry effect shown in fig. 3.6 is most important for electrons, because of their curved paths. The scattering in the dense wall could make the electron traverse the gas volume again, which would not be the case in a medium of uniform density. Kellerer estimates the re-entry rate of electrons with kinetic energies around 1 MeV is in the order of 20 % [59].

Graphical presentation of measurements

The low density of the gas and the proportional counter mode of the detector makes it very sensitive, being able to detect already a few ionizations. But also very large energy depositions can be measured, which allows the range of the lineal energy to span many, typically 5–8, orders of magnitude. This large dynamic range makes a

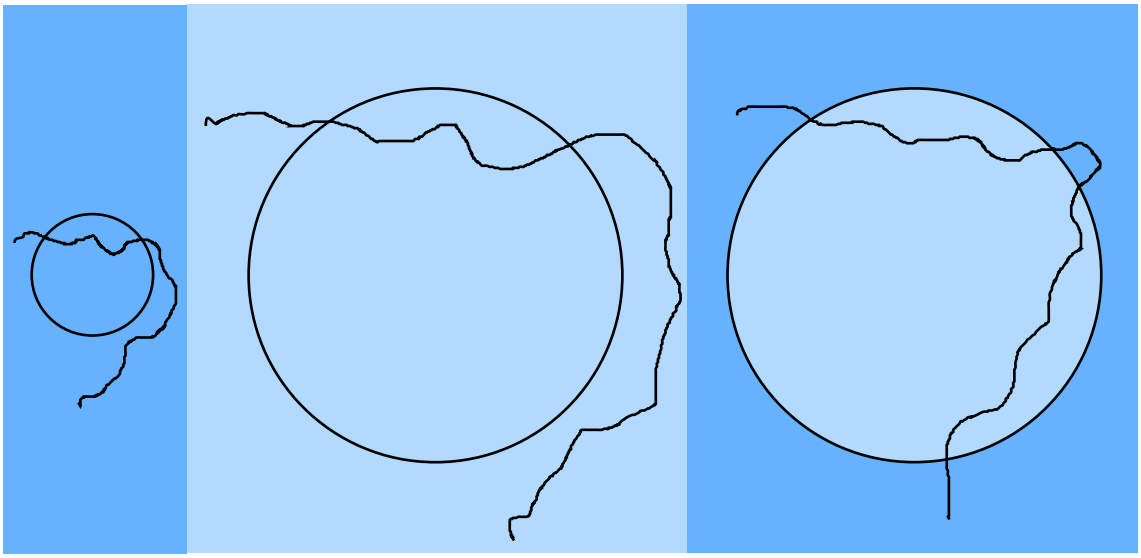

Figure 3.6: The re-entry effect.

logarithmic plot along the lineal energy axis necessary. Because

$$\int_{y_1}^{y_2} f(y)\,\mathrm{d}y = \int_{y_1}^{y_2} (y \cdot f(y))\ \mathrm{d}(\ln y) = \ln(10) \int_{y_1}^{y_2} (y \cdot f(y))\,\mathrm{d}(\log y), \tag{3.11}$$

the ordinate is multiplied with y in the semi-log representation.

The area limited by $[y_1, y_2]$ represents the fraction of events having values of y in that range. It is common in the community to weight the frequency distribution with y, making the area under the so-called *dose distribution in lineal energy* $d(y) = \frac{y \cdot f(y)}{y_F}$ express the fraction of total dose caused by events in the interval. An illustration of the different representations is given in fig. 3.7.

3.1.3 Applications

RBE estimation for radiation therapy

Microdosimetry has helped to establish models predicting the RBE for high-LET radiation, such as fast neutron therapy, boron neutron capture therapy (BNCT) and heavy ion therapy. For the latter, the microdosimetric kinetic model (MKM) [60, 61, 62, 63] has been developed by Hawkins and others and is successfully applied in treatment centers in Japan [14, 64]. The model combines elements of theory of dual radiation action [65], of the lethal-potentially lethal [66] and the repair-misrepair models [67] to predict the surviving fraction of cells from the dose deposited to volumes of subcellular size, independently of the radiation type.

It turned out that the dose-mean lineal energy, y_D (cf. eq. 3.5), is a good parameter to link the microdosimetric spectra to RBE values. To account for an decrease of the RBE for large y_D, similarly to the LET-RBE relation described in sec. 2.1.2, a saturated dose mean lineal energy, $y_{sat} = \frac{y_0^2}{y}\,(1 - \exp(-(y/y_0)^2))$ with $y_0 = 125\,\mathrm{keV\,\mu m^{-1}}$, was introduced by Kellerer and Rossi, transforming the dose mean lineal energy to:

$$y^* = \frac{\int_0^\infty y_{sat}\, y\, f(y)\,\mathrm{d}y}{\int_0^\infty y\, f(y)\,\mathrm{d}y} \tag{3.12}$$

Together with other model parameters depending on the tissue, a survival curve can be calculated, and, by comparing it to a reference survival curve, the RBE can be obtained [14, 68]. Newer extensions also regard the time structure of the treatment [69] and find a decrease of the RBE of several percent, if the treatment is prolonged or interrupted.

Radiation protection

Microdosimetric equipment has been in use in the field of radiation protection for a long time. Here, the biologically equivalent dose is needed to estimate the hazardousness of an unknown mixed radiation field in all areas where ionizing radiation is involved, e. g. in nuclear power plants, research centers, long-distance flights, but also in space radiation research, where the radiation exposure of astronauts is assessed.

The International Commision on Radiation Units and Measurements (ICRU) has established a framework to calculate the biolgically effective dose by introducing a weighting factor Q that the physical dose is multiplied with and that depends on the radiation quality [70]. In particular, Q depends on the lineal energy y, with a maximum at lineal energies around $100\,\mathrm{keV\,\mu m^{-1}}$. The International Commision on Radiological Protection (ICRP) uses the LET concept to state a relation of the weighting factor in depenance of the LET, with a similar relation [71].

3.2 Materials and Methods

3.2.1 Detector

For the measurements presented here, a spherical Rossi-type tissue-equivalent proportional counter (TEPC) is used. The original design was developed by Rossi [72], giving the detector its name. A thorough overview of the design of TEPCs is given in [58]. It is manufactured by *Far West, Inc.* and has a physical inner diameter of 1.27 cm (0.5 inch). As the name already suggests, it reaches its tissue equivalency by manufacturing the 1.27 mm (0.05 inch) thick wall from A-150 tissue-equivalent plastic [73], which is electrically conductive and has a composition similar to muscle tissue as defined by the ICRU, and by being filled with a propane-based gas mixture of almost the same atomic composition, cf. tab. 3.1. Apart from being as tissue-equivalent as possible, the gas also must provide a high gain for achieving good counting statistics. While propane-based gas has better gain properties and a composition closer to A-150 plastic, methane-based tissue-equivalent gas has an atomic composition more similar to the one of the ICRU muscle. The detector design is depicted in fig. 3.8. At a gas pressure of 88.5 hPa, this TEPC simulates a spherical volume of 2 µm of unit density.

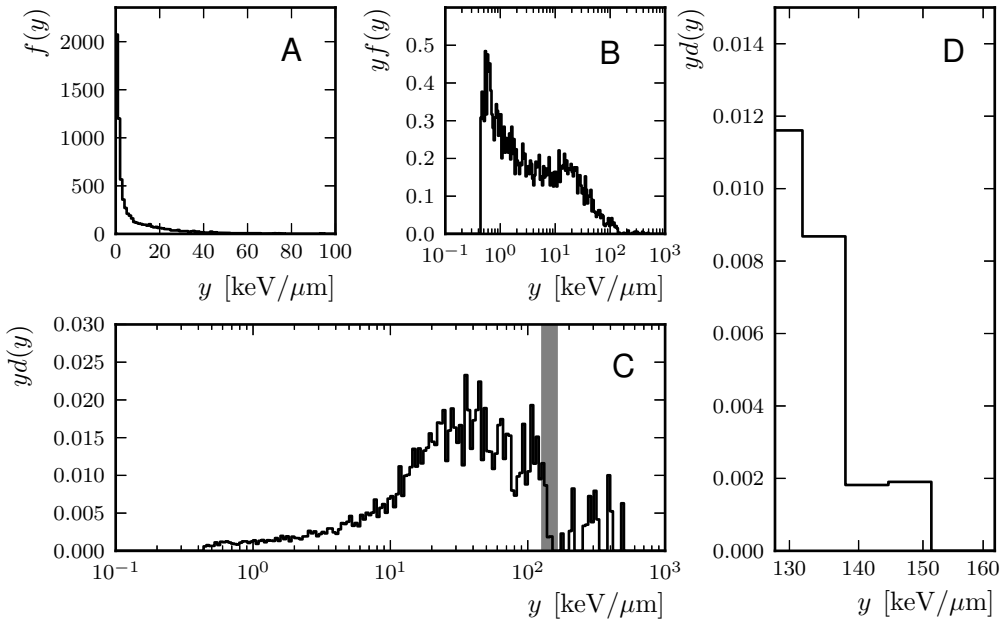

Figure 3.7: Microdosimetric spectra of neutrons from an Americium-Beryllium source. *A:* spectrum with linear horizontal axis. Events with lineal energies higher than about 40 keV/µm can not be seen in this representation. *B:* the same spectrum with logarithmic horizontal axis using the transformation in eq. 3.11. The area under the curve between two values of y represents the fraction of events, which lets conclude that e. g. about half of the events have lineal energies lower than approximately 3 keV/µm. *C:* instead of the fractional number of events, the area represents the fraction of dose delivered by events limited by two y values. Even though about half of the events have lineal energies lower than 3 keV/µm, about half of the dose is deposited by events with lineal energies larger than about 40 keV/µm. This measurement has been used to calibrate the horizontal axis using the *proton edge* feature described in sec. 3.2.4. Therefore, the scaling factor relating the hardware channel number of the measuring equipment to a lineal energy y was chosen such that the proton edge (gray area in *C*, zoomed in *D*) is at 150 keV/µm.

Element	ICRU muscle	A-150 plastic	Propane-based TE gas
H	10.1	10.2	10.3
C	11.1	76.8	56.9
N	2.6	3.6	3.5
O	76.2	5.9	29.3
F		1.7	
Ca		1.8	

Table 3.1: Atomic compositions (%) of muscle tissue as defined by ICRU, A-150 tissue-equivalent plastic and propane-based tissue-equivalent gas.

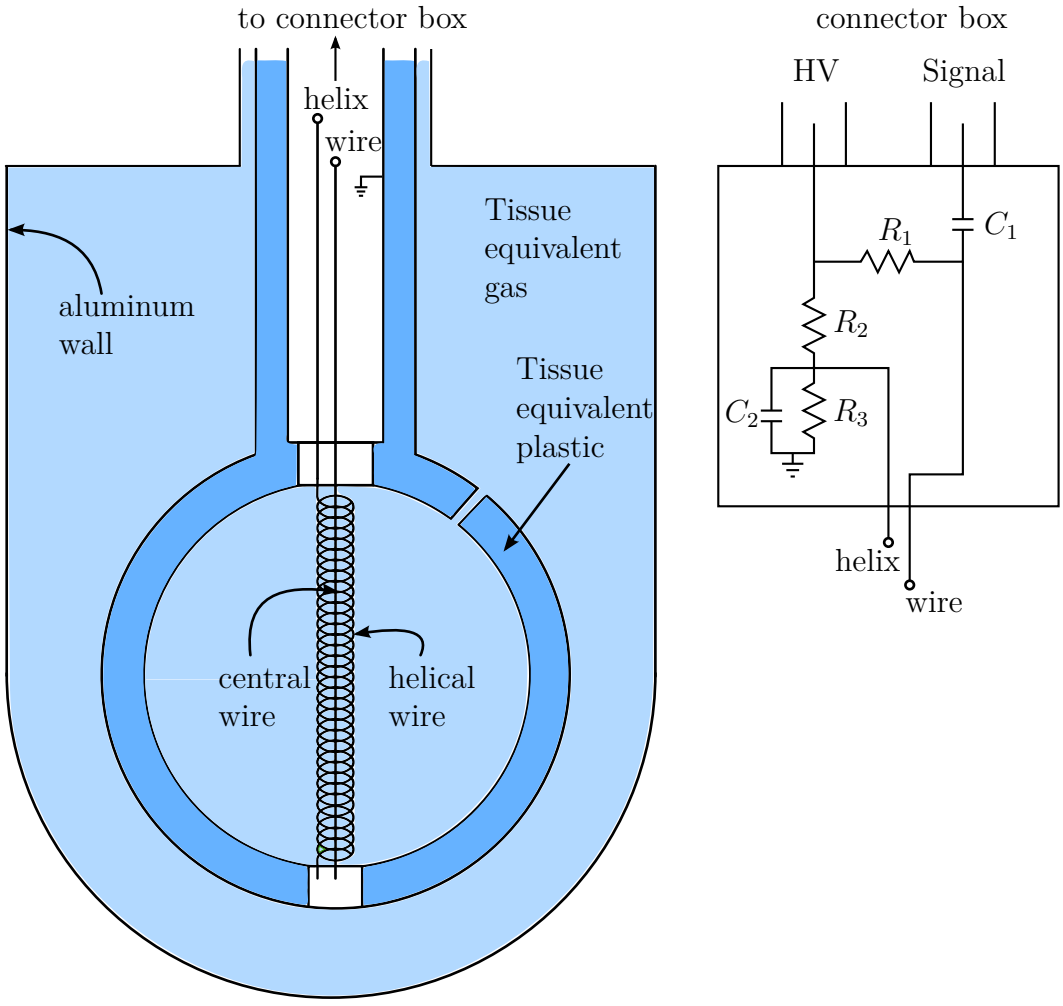

Figure 3.8: Tissue-equivalent proportional counter. The inner wire is encircled by a helix wire which generates the cylindrically symmetric electric field in the sphere. Both capacitors have 0.01 µF capacity, $R_1 = 3.9\,\mathrm{M\Omega}$, $R_2 = 30\,\mathrm{M\Omega}$, and $R_3 = 6.8\,\mathrm{M\Omega}$.

To achieve a uniform electric field, especially at the ends of the inner wire which are close to the wall, a wire helix around the inner wire confines the high electric field region close to the wire. This is where the acutal proportional region is located. 550 V are applied to the inner wire to collect the electrons from ionization events, and a voltage divider splits the voltage to the helix and the detector wall such that the avalanches occur between the helix and the wire and the remaining electric field between wall and helix is large enough to collect all ions. The power supply needs to have a very low noise voltage output, as the noise directly couples into the measured signal. Therefore, a *iseg SHQ 224M* power supply was used with a measured noise of less than 2 mV.

3.2.2 Read-out electronics

An overview of the read-out electronics setup is given in fig. 3.9.

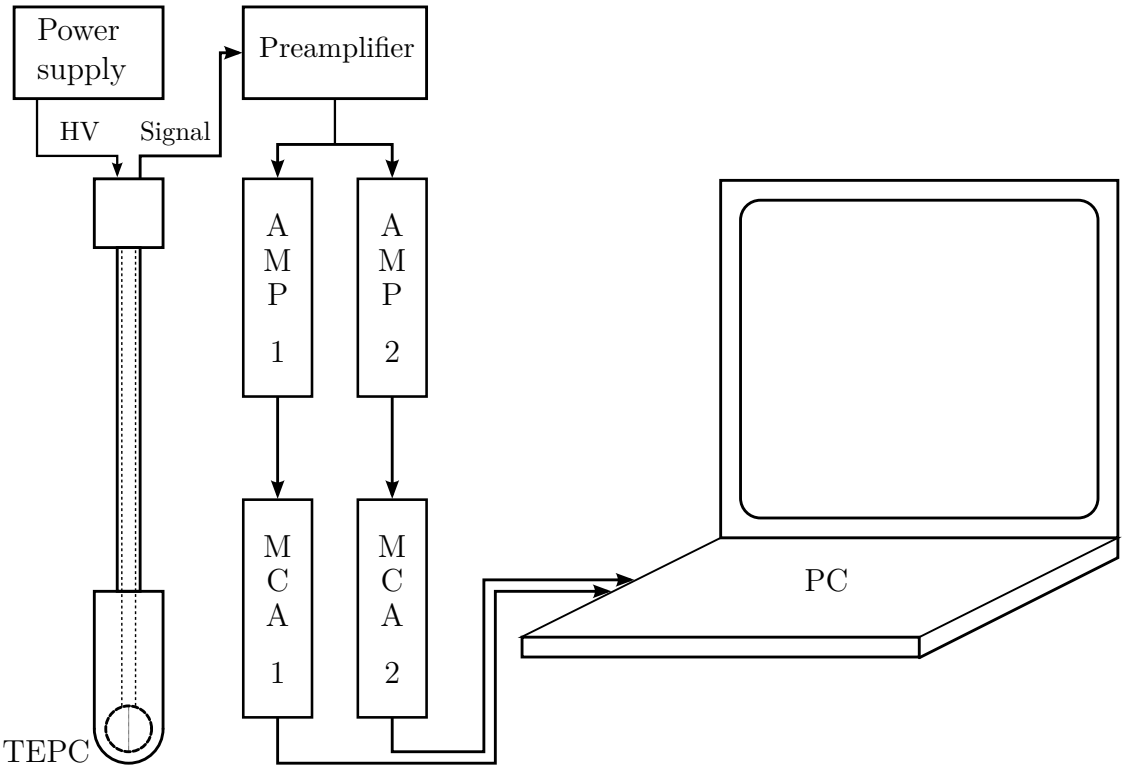

Figure 3.9: Electronics setup

Preamplifier

The signal of the TEPC is a negative charge pulse whose height is proportional to the energy deposited in a single event in the detector. In order to not couple ambient electromagnetic noise into the signal, a low-noise charge-sensitive preamplifier (*Canberra Model 2006*) is connected to the TEPC with a very short cable to convert the pulses into exponentially decaying voltage pulses with the height proportional to the primary ionization signal. The output pulses have positive polarity with a fast rise-time of less than 20 ns and a decay constant of 50 µs and are split in two, before they are fed into two spectroscopy amplifiers.

Spectroscopy amplifier

The two spectroscopy amplifiers integrate the preamplifier signals and provide additional amplification. Because the primary signal has a wide dynamic range, the signal from the preamplifier is fed into separate amplifiers having different gains to guarantee good resolution throughout the range. Three or even more amplifiers are recommended. In the setup used for the experiments presented in this work, two *ORTEC 572A* spectroscopy amplifiers were used with gains set to 10 and 100, respectively, to measure the high lineal energy events and also to have a good resolution for the low lineal energy ones. Their output is a quasi-gaussian shaped voltage pulse with amplitudes up to 10 V.

Multi-channel analyzers, data acquisition

The amplified signals are fed into two independent multi-channel analyzers (*ORTEC Aspec 927*), each having 16384 channels. They convert the pulse height from the spectroscopy amplifiers into a channel number which is binned in a histogram on the screen of a connected computer. These histograms can be saved and represent the raw data for the following analysis.

3.2.3 Data processing

A self-written routine is used to read in the raw data and do the necessary processing to yield the lineal energy spectra in frequency and dose, respectively, and the

associated moments of the distributions. The two spectra are merged and the channel numbers converted into a linear energy scale with conversion factors obtained in a calibration measurement (cf. sec. 3.2.4). Afterwards, the data is rebinned onto a logarithmic horizontal axis with the transformation described in sec. 3.1.2. Finally, the moments of the distribution are calculated and the histograms are displayed and saved.

3.2.4 Calibration

The raw data as displayed in the data acquisition software is proportional to the lineal energy, but the proportionality factor has to be determined in a calibration measurement. There are several methods for calibrating a TEPC, each involving irradiating the detector with radiation that imparts well known amounts of energy.

The most convenient calibration method for high-LET radiation is to have a small radioactive ^{244}Cm or ^{241}Am alpha source built into the detector. The geometry of the emission is known, the energy loss of the particles in the cavity can be calculated, thus a relationship between channel and lineal energies can be established. However, this method has systematic uncertainties in the order of 10 % because of uncertainties in the initial kinetic energy (due to the finite source thickness) and unknown details about the geometrical path of the particles (for more details cf. [74]). Furthermore, the manufacturer of the TEPC used for the experiments presented here experienced a supply bottleneck with radioactive sources, thus another calibration procedure was used.

Neutrons with kinetic energies above several 100 keV, e. g. from an Americium-Beryllium (AmBe) source, impart energy into the TEPC by recoiling protons which they create essentially in inelastic collisions with the wall material. These secondary protons have a broad energy distribution, depending on the kinematics of the collision. However, there is a maximum possible energy a proton can deposit in the detector. This is the case if it has just enough energy to traverse the gas along a full diameter, stopping right before the opposite wall. Protons with less energy naturally deposit less energy, those with higher kinetic energies carry away some energy that is deposited elsewhere. Hence, there is a sharp drop in the measured spectrum that is called the *proton edge*. To stop after traversing 2 µm of ICRU muscle medium, a proton needs initially about 150 keV kinetic energy (projected range looked up in PSTAR [75]), making the proton edge appear at $y = 150\,\mathrm{keV/\mu m}$.

However, also heavier recoiling nuclei are created and energy and range straggling of the protons blur the edge, which gives rise to an estimated uncertainty of the proton edge position of ±10 keV/µm. The setup and measured spectrum is shown in fig. 3.7 (sub-figures *C* and *D*).

3.2.5 Measurement environment at Heidelberg Ion-Beam Therapy Center (HIT)

General features of the facility

HIT is a clinical facility to provide the entire environment for treating cancer patients with proton and carbon ion beams. The accelerator section consists of two independent ion sources, a linear accelerator section, and a synchrotron which is capable to deliver protons at energies between 48 and 221 MeV and and carbon ions with energies between 89 and 430 MeV/u, respectively. The ions are then transferred to several treatment rooms where they are deflected by a pair of horizontal and vertical magnets to scan the lateral extensions of the tumor with the beam. Two of the treatment rooms provide beam exits in a horizontal direction and a third room is equipped with a gantry that is able to rotate the beam 360° around the patient. Further degrees of freedom are patient positioning, the choice of the beam size, and its current. All beam parameters are stored in a hardware library, such that any possible combination can be requested within one synchrotron cycle. The measurements presented here were carried out in an additional room, the quality assurance room, which is technically equivalent to a horziontal treatment room. Because the standard currents used for patient treatment are rather high to save time (up to about 10^{10} particles per second for protons and 10^8 particles per second for carbon ions, respectively), even the lowest possible current available in the hardware library was by far to high to measure single-event spectra. Hence, to avoid pile-up in the spectra, the beam current was manually reduced by changing the deflection strength of a magnet in the source section of the accelerator chain. The currents needed for the experiment were so low such that the signal of the beam monitoring system which is used to correct for position deviations and to measure the number of particles delivered during treatment was below threshold. This made it impossible to record the current pattern during beam extraction, thus ensuring a constant beam. Because no other detector able to measure the beam intensity was available,

the current was lowered to the lowest value possible, such that the next lower setting resulted in no measureable signal at all; still it can not be entirely excluded that during limited amounts of time, the beam current was too high, producing pile-up events.

3.2.6 Active and passive beam delivery

As mentioned in the introduction of this chapter, the aim of this study is to asses the ability of the detector to monitor differences in the spectra of ion beams for passive and active delivering systems. HIT is an active system by design, as described in the section above. The only material in the beam is the vaccum exit window, a set of three ionization chambers sandwiched between two multi-wire proportional counters used for the treatment control system,[1] and an optional ripple filter, which is used to widen the width of the Bragg peak by inserting a plastic plate with a thickness of 3 mm that is thinned down in a peridodic ridge-like pattern, such that different parts of the beam traverse a slightly different amount of material, making them stop at slightly different depths.

Compared to a passive beam delivery system, this is still very little material. The passive technique most often has a cyclotron accelerating the beam to a fixed energy that has to be high enough to penetrate about 20–30 cm into tissue to be able to reach any position in the patient. For target volumes that are located more in front, the excess beam energy has to be taken away again by degrader material (cf. fig. 3.10) that is put into the beam path. Some manufacturers of commercially available therapy accelerators introduce an energy selection system that uses magnets to filter away the secondary particles produced from the reactions in the degrader. However, additional material of varying thickness is needed to modulate the Bragg peak position along the beam direction, i. e. to produce a spread-out Bragg peak. This is usually realized by a spinning wheel with different thicknesses of material mounted on it. Afterwards, the beam is widened by specially designed scatter devices, before it is collimated again to the lateral target shape by patient-specific collimators. Consequently, the beam is always impinging the target volume on its whole lateral extension at once, contrary to the active case, where a thin beam is scanned over

[1] It actually turns out that for low extraction energies there is a substantial influence of the tungsten wires of the multi-wire proportional counters that are used to verify the beam's position, cf. [76]

the volume. The last element in the beam delivery system is a patient-specific compensator consisting of a plastic block with a specially milled pattern to match the range of the particles to the shape of the rear part of the target volume. At least the last three elements mentioned are on the same axis as the patient, such that all the secondary particles generated in inelastic scatterings with these materials could potentially reach the patient and deliver unwanted dose. Especially neutrons are dangerous because of their enhanced biological effect throughout their range.

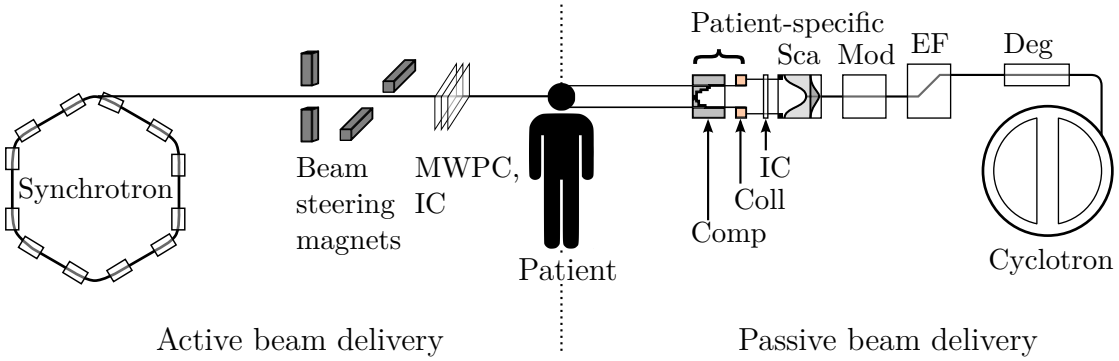

Figure 3.10: Active and passive beam delivery. Sizes and distances not to scale. The half picture *left* of the patient shows the active beam delivery case, the *right* half shows the passive case. Abbreviations along beam direction: Active: *MWPC:* multi-wire proportional counter for beam position measurement, *IC:* ionization chamber. Passive: *Deg:* degrader, *EF:* energy selection system and filter, *Mod:* modulator, *Sca:* scatterer, *IC:* ionization chamber, *Coll:* patient-specific collimator, *Comp:* patient-specific compensator. Further explanations are given in the text.

3.2.7 Design idea of the experiment

All experiments for the study presented here were carried out at the Heidelberg Ion-Beam Therapy Center (HIT), which has, as mentioned above, active beam delivery. Microdosimetric spectra are taken in the plateau region as well as in the Bragg peak for carbon ions and protons, respectively. The energies of the particles were chosen such that their range in water is the same for both particle types.

The passive environment is mimicked by choosing the highest possible extraction energy at the synchrotron and passively degrade the energy by 17.5 cm of PMMA, such that the beam energy after the degrader is the same as in the active case.

3.2.8 Setup

The TEPC was placed in a water phantom that is also used for routine quality assurance measurements. Its walls are made of PMMA and the front window is thinned down to 5 mm. The detector was mounted onto a 3D translation stage with a positioning accuracy of 0.1 mm to be able to measure at different well-defined depths.

The center of the TEPC in its frontmost placement on the central axis of the phantom was made to conincide with the origin of the room's coordinate system, the so-called isocenter, by moving the water phantom. In this configuration, the beam exit window was at 1.4 meters upstream from the center of the detector, and the distance to the inner surface of the front window was 3 cm (cf. fig. 3.11). This position is the plateau position presented in the results later. The other position was at 9.5 cm behind the front window, the position of the Bragg peak as calculated using measured range tables that were available at the facility.

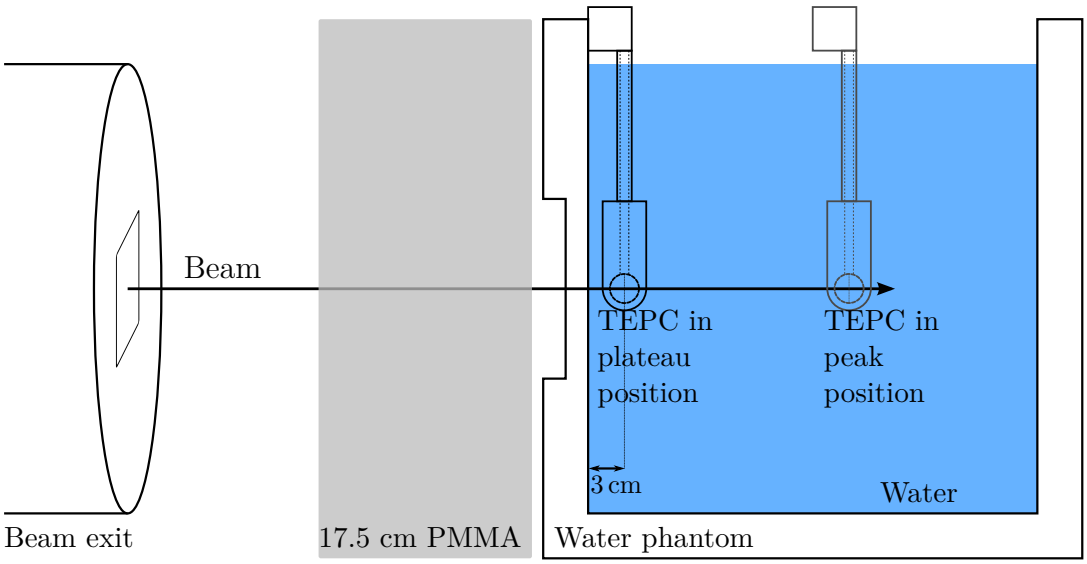

Figure 3.11: Measurement set-up. The left position of the TEPC is regarded as the plateau in the results presented later, the shaded position corresponds to the Bragg peak measurement. To mimick the passive beam delivery scenario, a 17.5 cm thick PMMA block was put in front of the phantom.

The detector was connected to the read-out electronics as described in sec. 3.2.2. The noise at the output connector of the preamplifier was typically less than 3 mV,

but was critically influenced by external factors. For example, simply changing the position of the preamplifier increased the noise by several millivolts. Furthermore, other electrical devices such as the 3D translation stage had to be powered off because they coupled in substantial noise. Finally, the detector is very susceptible to microphonic noise, in such an extent that the vibrations of the connected power supply's imbalanced fan originally introduced massive oscillations in the preamplifier's output. The power supply was repaired before the actual measurements were carried out.

As described in sec. 3.2.7, the passive beam delivery environment is mimicked by inserting 17.5 cm of PMMA in front of the water phantom and increasing the ion energies to the maximum the accelerator could deliver. For carbon ions, a 3 mm ripple filter was used in the Bragg peak position. All beam parameters are summarized in tab. 3.2.

	p, active	p, passive	C, active	C, passive
Energy (MeV/u)	120.05	221.06	226.05	430.10
FWHM (cm)	1.65	1.26	1.03	0.98
PMMA thickness (cm)	0	17.5	0	17.5
Ripple filter active?	no	no	yes, in Bragg peak	yes, in Bragg peak

Table 3.2: Beam parameters

As the lineal energy is defined as the ratio of energy imparted and the mean chord length, it has to be noted that the mean chord length in the experiment described here is different from $2/3\,d$, which is, as mentioned earlier, only true in isotropic irradiation or, because of symmetry reasons, an irradiation by a broad beam. The latter condition is not fulfilled here, because the beam shape is gaussian and its width is narrow, which is needed to precisely deliver dose to the tumor for treatment purposes. To reduce this influence as much as possible, the widest possible width (about 1 cm full width at half maximum, depending on particle type and energy, cf. tab. 3.2) was chosen. Because of limited measurement time, the workaround by scanning the beam over an area larger than the cross section of the detector, thus averaging out the beam shape, could not be carried out.

The data acquisition time for each measurement presented here took about 20 minutes, such that typically about 50 000 events were recorded.

3.2.9 Monte-Carlo simulations

To compare the experimental findings with simulated data, the setup was also modeled using the Monte-Carlo code *FLUKA* version 2011.2b. Because multi-purpose Monte-Carlo codes like *FLUKA* use a standard set of parameters that balance the accuracy of the results with the time needed to complete a simulation, the thresholds for production and transport of secondary particles are by default set too high to yield reasonable microdosimetric spectra, in particular to correctly account for effects like the wall effect described in sec. 3.1.2 and the accurate production and transport of low-energy secondary electrons that are potentially able to travel into the wall before they are stopped. With the thresholds set too high, electrons in the sensitive volume could be stopped by the code too early when reaching the transport threshold energy, even though they would be energetic enough to deposit a significant amount of their energy in the wall. As a result, the code deposits all of their residual energy into the sensitive volume, which would bias the results. Therefore, the thresholds for the 'HADROTHErapy' set of initial parameters were lowered manually in regions where they are relevant for the simulated results, i. e. in the inner parts of the TEPC wall and its sensitive gas volume. Because production and transport thresholds can be set for each material in *FLUKA*, the TEPC wall is realized as onion-shaped structure like proposed in [77] (cf. fig. 3.12), consisting of three concentric shells, to compromise between accurate results and the significant increase of computation time needed for low thresholds. The A-150 tissue-equivalent plastic material is duplicated for each shell, maintaining the atomic composition, but lowering the production and transport threshold for electrons step by step from the default value of 100 keV in the outer shell, to 10 keV in the middle shell, and 1 keV in the innermost shell as well as in the gas inside of the detector. The widths of the shells were chosen according to the ranges given by the continuous slowing down approximation (csda) model for electrons [75] in A-150 plastic.

A major benefit of Monte-Carlo simulations is that they generally yield additional information about the data. In the results presented here, not only the microdosimetric spectra are simulated like in the experiment, but also the relative contributions of all particle species involved are displayed. Secondary electrons with a kinetic energy exceeding an internal threshold are treated as independent particles in the code. If an event only contains energy contributions by the primary beam particle and electrons, the electron energy was merged into the energy contribution

of the primary particle. This is done because the amount of energy carried into the detector by electrons generated outside the detector by other secondary particles is estimated to be very small. Remaining electron contributions are regarded as originating from the other particle species occuring in the detector.

For every scenario, 10^5 to 10^6 primary particles have been simulated, such that at least 10^5 events were recorded in the detector in every simulation.

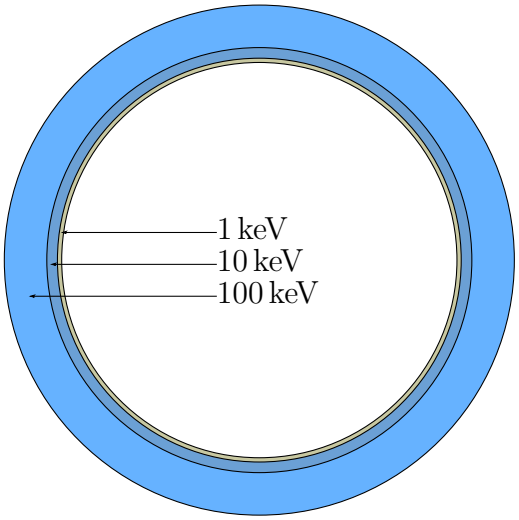

Figure 3.12: Onion-like implementation of the TEPC in the Monte-Carlo simulations. The production and transport cut-off values of *FLUKA* are lowered for each shell to guarantee as accurate particle transport as possible while maintaining a reasonable computation time.

3.3 Results

3.3.1 Measurements

Each plot shows the dose distributions in lineal energy both for the active as well as the passive scenario. Because the differences in the spectra are too small to be visible if presented in the standard way (cf. sec. 3.1.2), also the vertical axis is transformed into logarithmic scale.

Protons

Protons, being singly charged, have a lower stopping power compared to carbon ions (cf. eq. 1.2). Consequently, the majority of events in the dose distribution in lineal energy plotted in fig. 3.13 have low lineal energies in the range between 0.4 and 10 keV/µm. The events with lineal energies higher than 10 keV/µm are due to heavier nuclei that were generated in inelastic scattering events, or pile-up events which could be due to a momentary too high particle rate due to the inhomogeneous particle extraction at the synchrotron.

For the plateau, the peak at about 0.6 keV/µm in the upper spectrum of fig. 3.13 matches the stopping power for protons in this energy interval. The stopping power of protons in the Bragg peak is about 80 keV/µm; events with lineal energies in this range do not appear in the spectrum in the lower part of fig. 3.13. Due to the limited time available for the measurements, neither a depth scan of the detector was carried out to find the Bragg peak position, nor a spread-out Bragg peak was chosen to irradiate it with. Instead, the detector was placed on a position where the Bragg peak was estimated from range calculations available at the facility. The lack of high lineal energy events and the similarity to the plateau spectrum suggests that the actual measurement position was in front of the Bragg peak. However, as the aim of the measurement is to reveal possible differences in the spectra due to additional secondary particles generated in passive delivery systems, it is possible to conclude that, in the irradiated volume, the difference between the two spectra is negligibly small. Yet, statistical significance is too low to argue if there is a significant difference in the events with lineal energies higher than 20 keV/µm. The frequency and dose mean lineal energies are summarized in tab. 3.3.

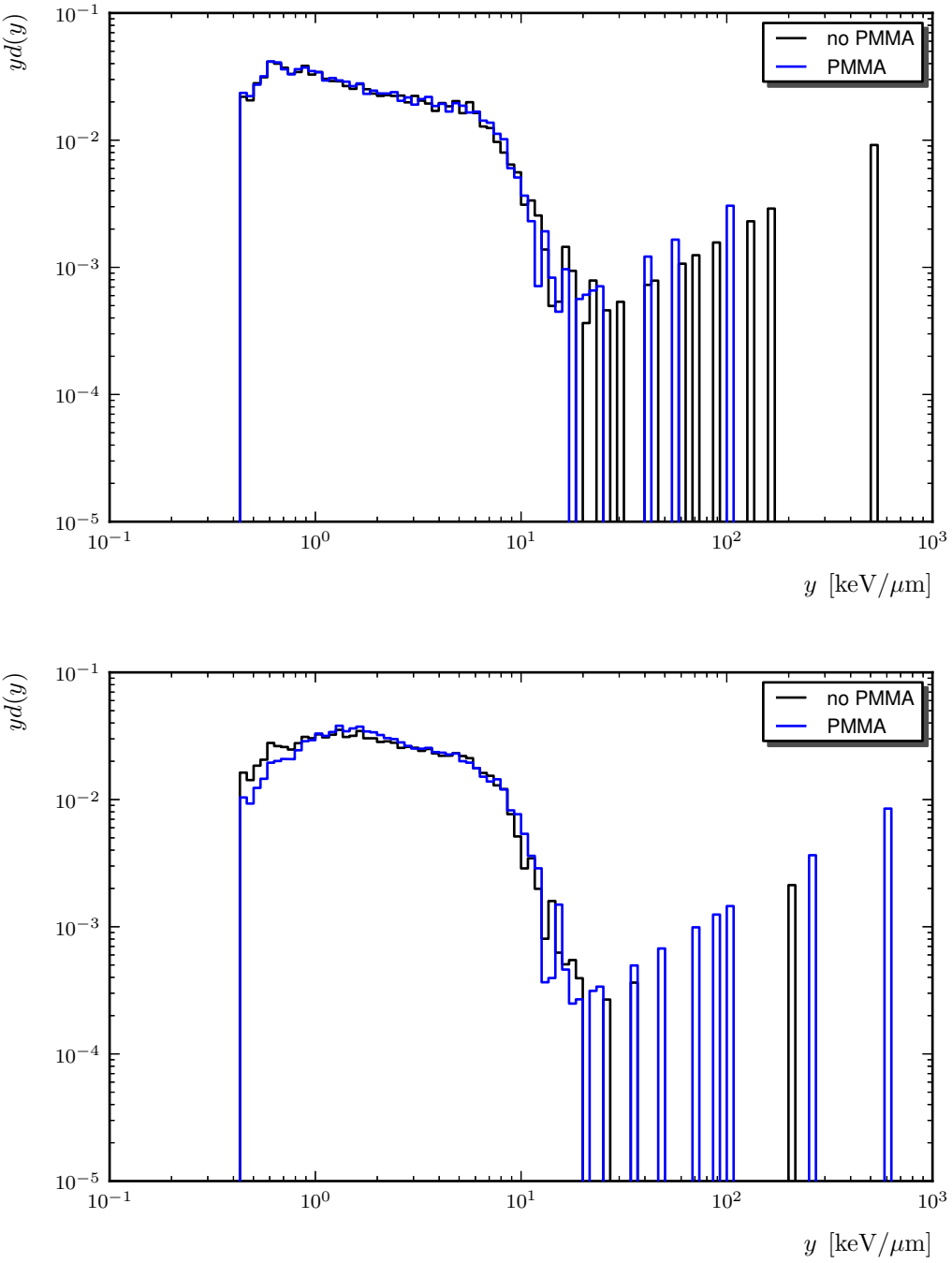

Figure 3.13: Dose distributions in lineal energy for protons. *Top:* plateau. *Bottom:* estimated Bragg peak position.

Carbon ions

Because of their higher charge, carbon ions have higher a stopping power along their range than protons. Also here, the peak in the spectra for the plateau case matches the stopping power of about 16 keV/µm. For the passively degraded case, a clearly visible, however not substantial (logarithmic scale) difference appears at lineal energies lower than 10 keV/µm, where a larger fraction of the total dose is delivered by events with lower lineal energies as compared to the active case. This is due to fragmentation, i. e. brake-up of the primary carbon ion beams in the PMMA degrader in inelastic scattering processes, where secondary particles with lower charge and, therefore, lineal energies are created.

As the energies of carbon ions were chosen to have the same range as the above mentioned protons, the Bragg peak position was also likely missed here. This is substantiated by the fact that the observed maximum in the spectrum of lineal energy events is at about 40 keV/µm, which is, even though enhanced as compared to the plateau case, significantly lower than expected for the Bragg peak (several 100 keV/µm). The fragmentation of the primary carbon ions is also visible for the active case, as the actively delivered ions as well undergo inelastic scattering processes with the water. Consequently, the differences between the two spectra are not as large as in the plateau case.

Similarly to the measurements with protons, despite the difference for lower lineal energies explained already, there is no large difference between the results for the different beam delivery scenarios. As in the case for protons, more statistics is needed to make profound statements about the significance of the differences. The frequency and dose mean lineal energies are summarized in tab. 3.3.

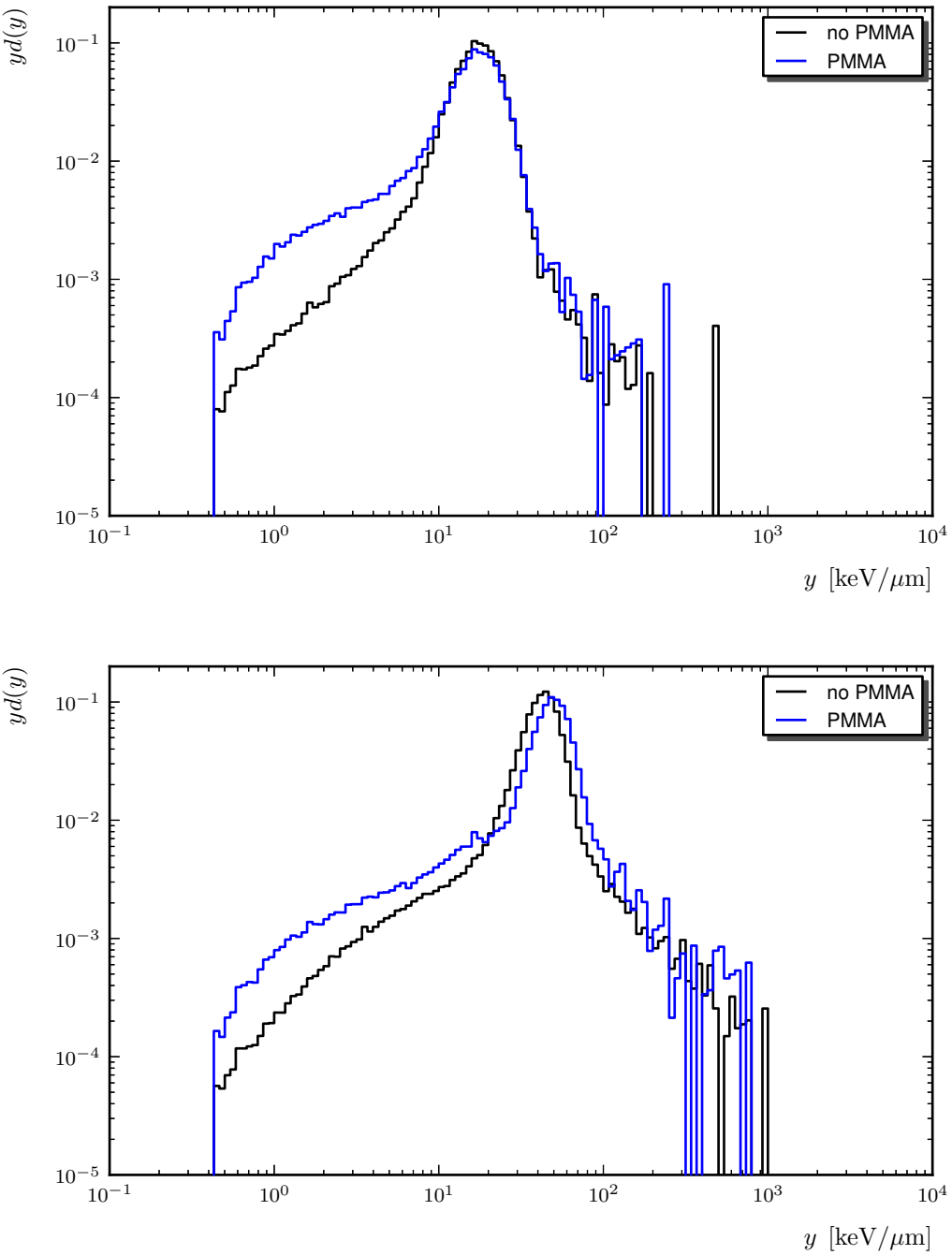

Figure 3.14: Dose distributions in lineal energy for carbon ions. *Top:* plateau. *Bottom:* estimated Bragg peak position. The shift of the peak in the spectra is attributed to inaccuracies of the calculated PMMA width, resulting in a slightly different initial kinetic energy of the primary ions. In the region in front of the Bragg peak, where the stopping power increases rapidly, these small differences result in a shift of the spectrum towards higher lineal energies.

Particle	Position	PMMA?	y_F (keV/µm)	y_D (keV/µm)
Proton	Plateau	no	1.2	8.3 (*)
Proton	Plateau	yes	1.2	2.8
Proton	"Bragg peak"	no	1.4	3.1
Proton	"Bragg peak"	yes	1.5	9.2 (**)
Carbon	Plateau	no	13.9	17.9
Carbon	Plateau	yes	9.5	16.8
Carbon	"Bragg peak"	no	28.5	45.6
Carbon	"Bragg peak"	yes	21.4	50.5

Table 3.3: Frequency (y_F) and dose (y_D) mean lineal energies for the measurements. The position "Bragg peak" corresponds to a position in front of the Bragg peak, as described before. Because of the low statistics, y_D is heavily influenced by outliers, such that the two rightmost peaks in the proton measurements are responsible for the rather high values in (*) and (**).

3.3.2 Simulations

As mentioned in sec. 3.2.9, the experiment was also carried out in-silico, i. e. in a Monte-Carlo simulation. Here, the detector could be positioned exactly at Bragg peak depth. Furthermore, not only the total dose spectrum in lineal energy was calculated, but also the individual contributions of every particle species from protons up to oxygen ions to gain a deeper insight into the composition of the spectra. For the plateau cases, the spectra also include the measured data. In tab. 3.4, the mean values are summarized.

Protons

Like in the experiment, there is not much difference between the active and passive scenario in the plateau case, cf. fig. 3.15. The events with higher lineal energies are due to heavier particles generated in inelastic collisions and are slightly more pronounced in the passive scenario, particularly the contribution of carbon ions. The spectra for the measured data were scaled down to account for the lack of signal below the 0.4 keV/µm threshold and are, within their limited statistics, compatible with the simulation.

Larger differences between the scenarios appear in the Bragg peak (fig. 3.16): the spectrum for the passive case is broadened both to lower and higher lineal energies

and the higher lineal energies have a larger amount of contributions of heavier particles. Consequently, the simulations suggest that there is a difference that can be seen in the measurements, provided that enough statistics is collected.

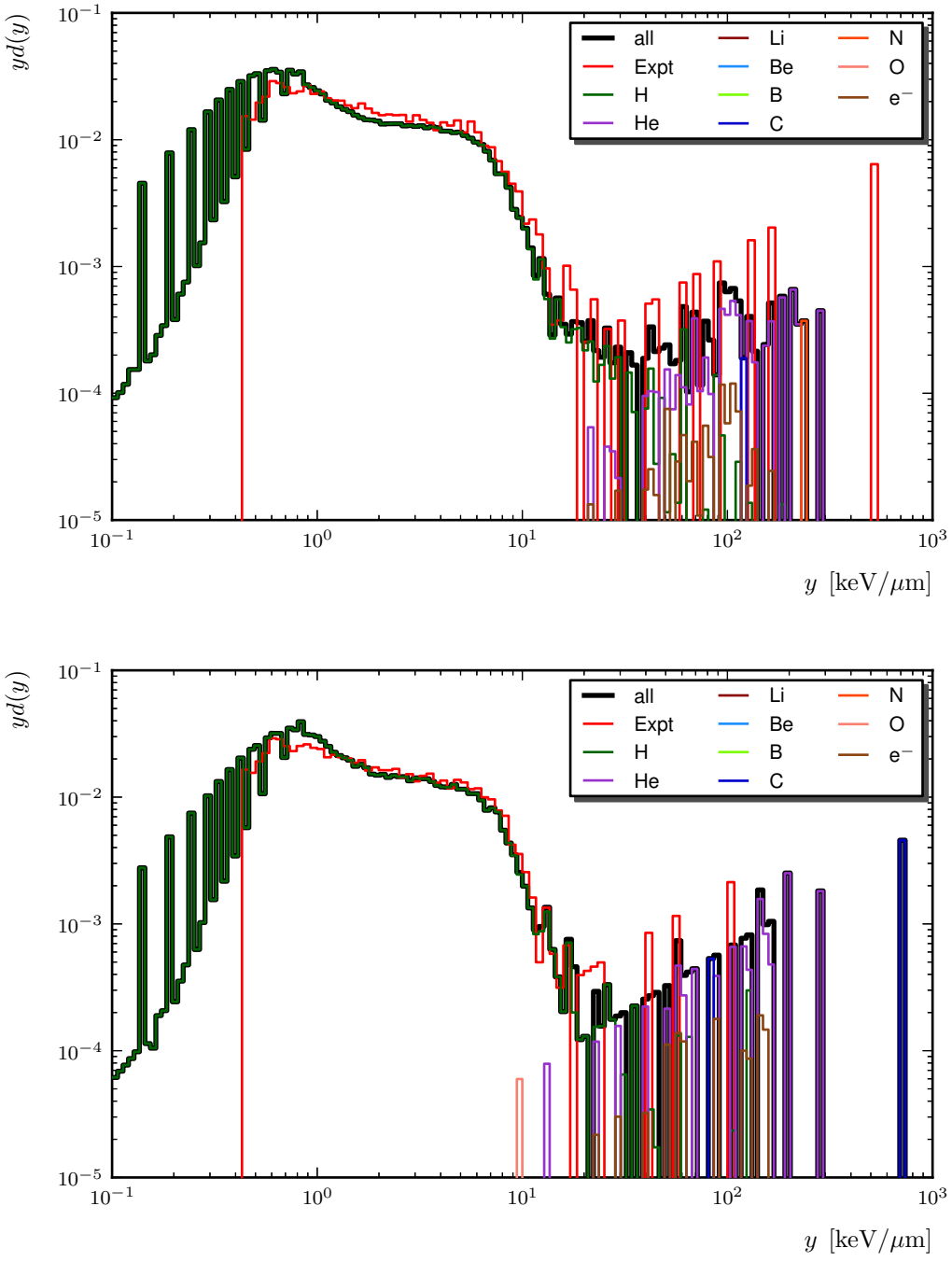

Figure 3.15: Dose distribution in lineal energy for protons in plateau. *Top:* active beam delivery. *Bottom:* passive delivery.

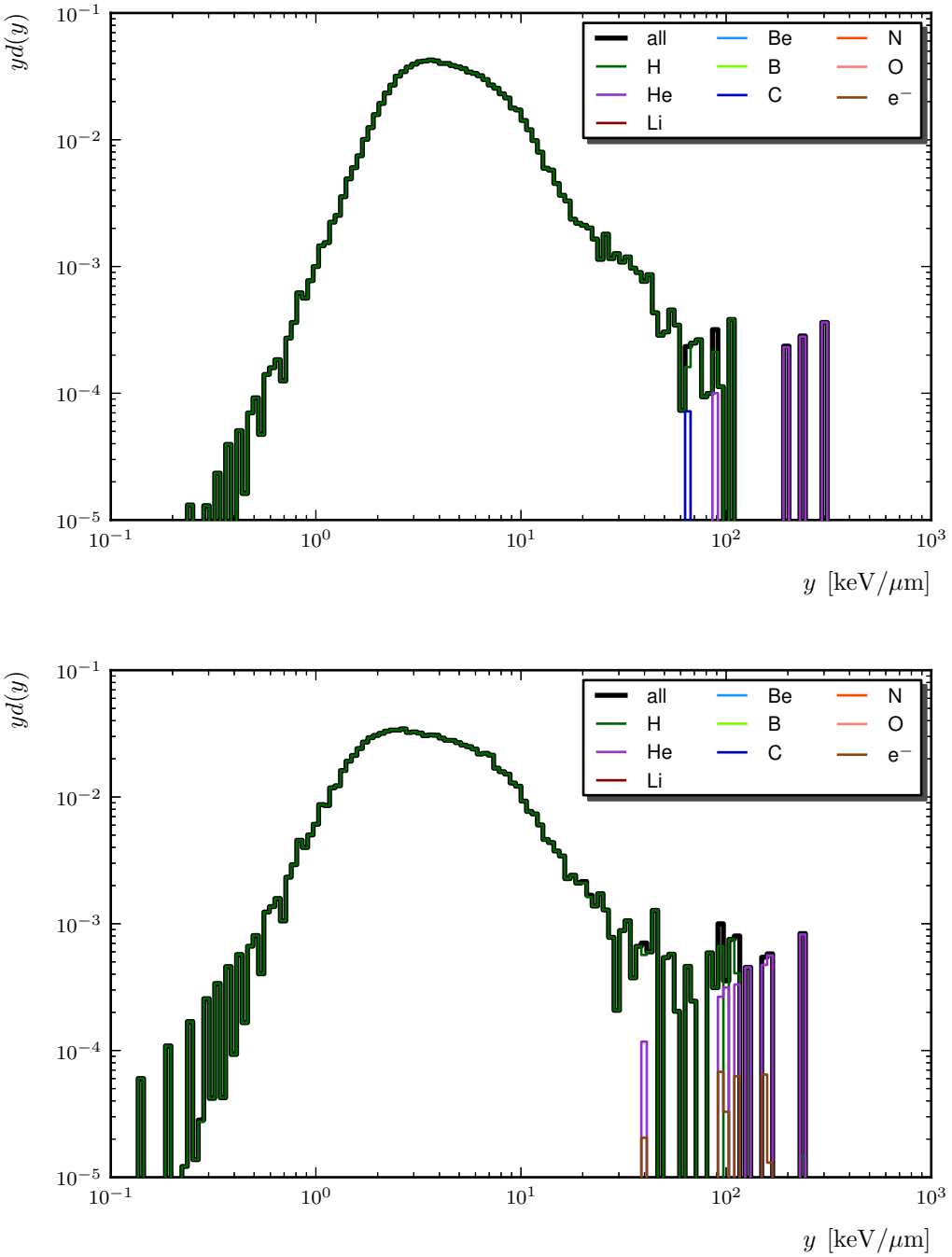

Figure 3.16: Dose distribution in lineal energy for protons in Bragg peak. *Top:* active beam delivery. *Bottom:* passive delivery.

Carbon ions

Being compound nuclei, carbon ions are able to lose neutrons and protons in inelastic scattering processes with the traversed material. Consequently, they appear as different elements if their atomic number has changed. Thus, compared to protons, the contribution of other particle species to the total spectrum is larger.

In the plateau, the spectrum for the passive case extends both towards lower and higher lineal energies as in the active scenario, as can be seen in fig. 3.17. Furthermore, the relative contribution of fragments is enhanced. Except for slight deviations in the peak position and height, the measured spectra agree well with the simulated ones.

High lineal energies in the Bragg peak are almost exclusively due to the carbon ions, because of the z^2 dependence of stopping power and the lack of even higher charged particles produced in inelastic processes. However, the shapes of the spectra in the high y region differ significantly when comparing the active and passive scenario (cf. fig. 3.18): there is a larger contribution of lineal energies at about 100 keV/µm in the active case, whereas in the passive case, there are more events with even higher lineal energies.

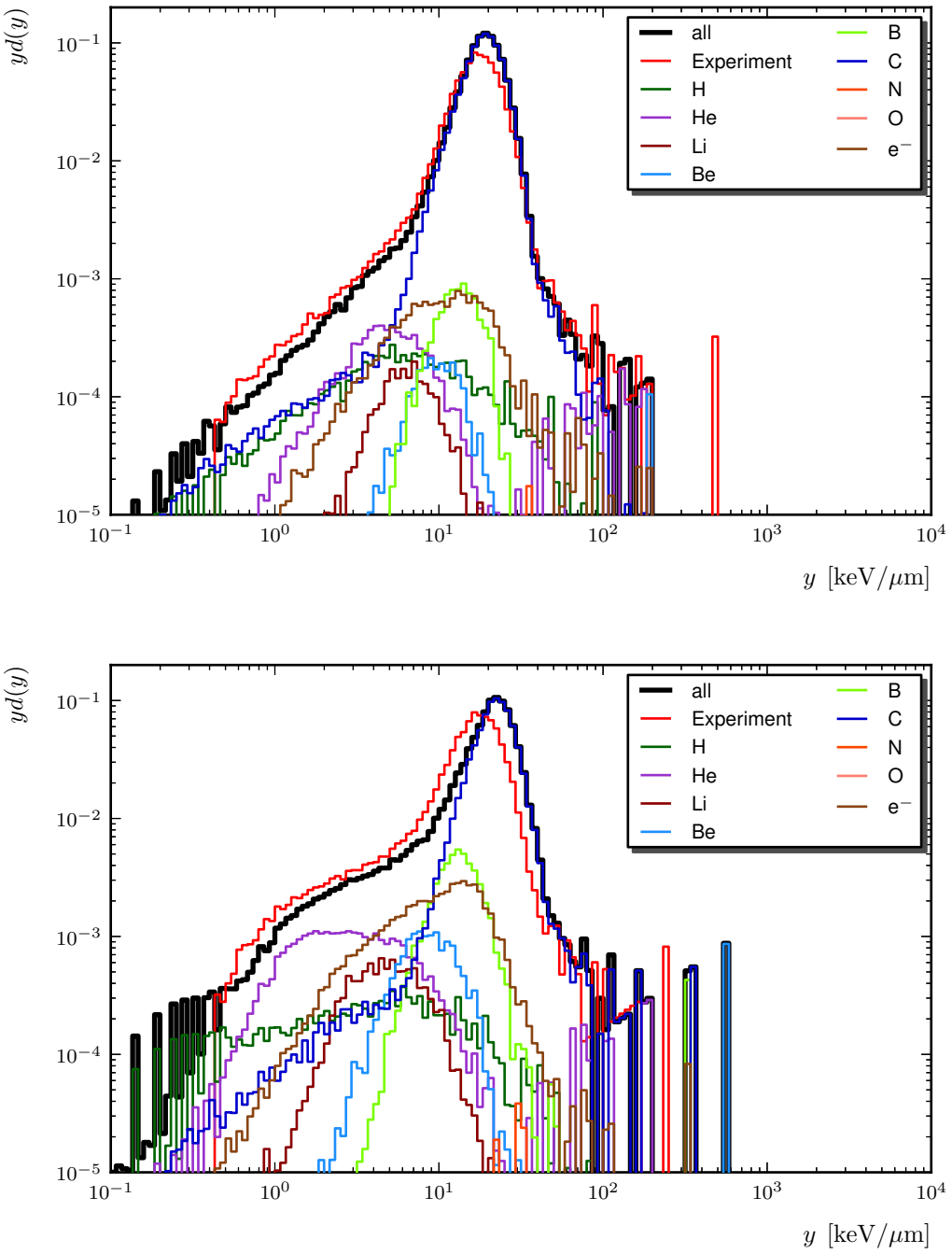

Figure 3.17: Dose distribution in lineal energy for carbon ions in plateau. *Top:* active beam delivery. *Bottom:* passive delivery.

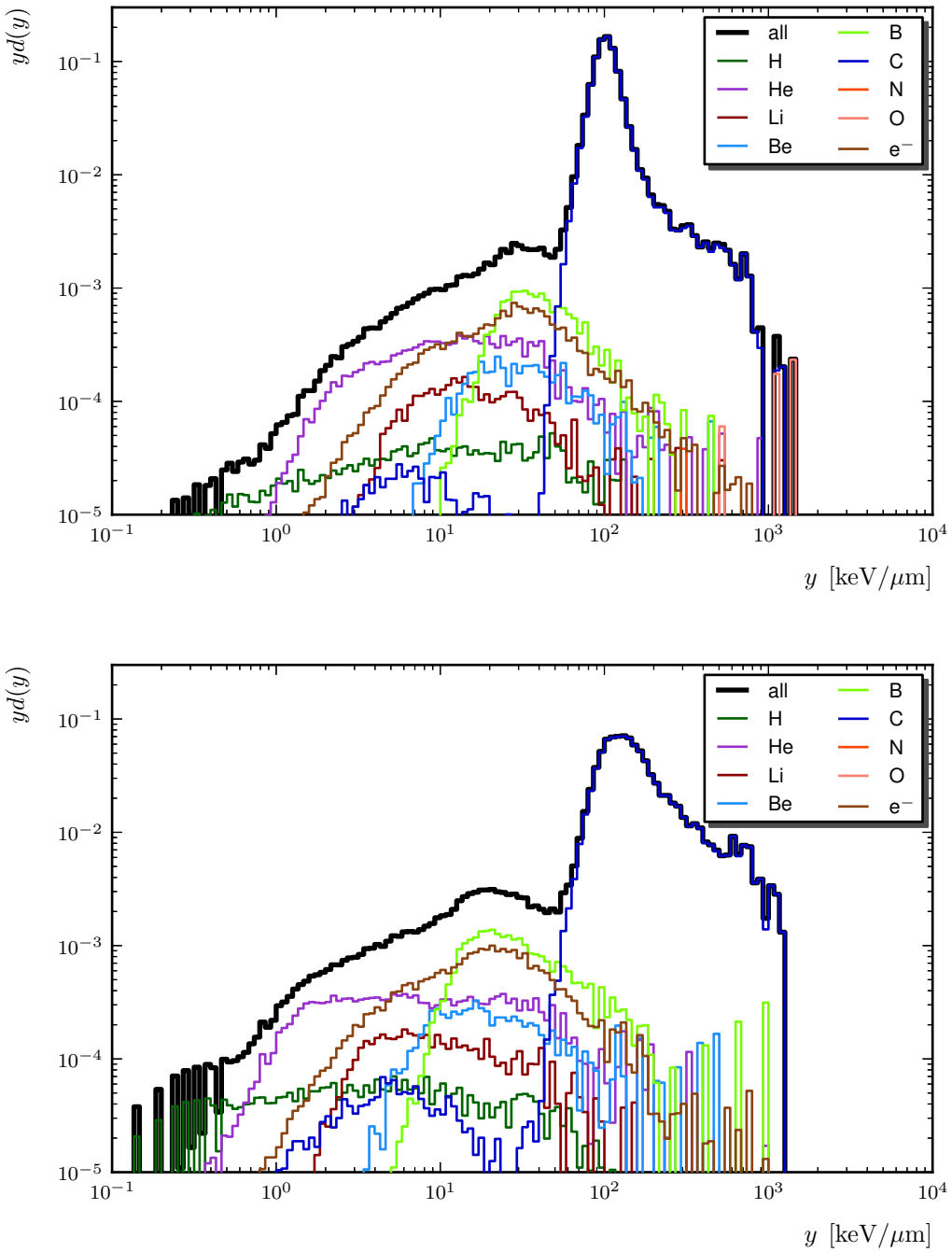

Figure 3.18: Dose distribution in lineal energy for carbon ions in Bragg peak. *Top:* active beam delivery. *Bottom:* passive delivery.

Particle	Position	PMMA?	y_F (keV/µm)	y_D (keV/µm)
Proton	Plateau	no	0.8	3.1
Proton	Plateau	yes	0.9	99.2 (*)
Proton	Bragg peak	no	3.8	5.9
Proton	Bragg peak	yes	2.7	5.4
Carbon	Plateau	no	15.4	19.0
Carbon	Plateau	yes	10.9	21.43
Carbon	Bragg peak	no	68.5	116.3
Carbon	Bragg peak	yes	46.4	183.6

Table 3.4: Frequency (y_F) and dose (y_D) mean lineal energies for the simulations. As in tab. 3.3, y_D in (*) is influenced by the outlier at 700 keV/µm in fig. 3.15, making its value very high.

3.4 Discussion

The results presented in sec. 3.3.1 were obtained in an experiment that was planned as a precursor to a more thorough measurement. Unfortunately, the main experiment was cancelled due to a lack of beam time caused by extensive procedures to install important upgrades at the HIT facility.

Comparing the spectra of the measured distributions indicates no large difference between the active and passive beam delivery scenario and longer running times of the experiment would be needed for a final proof of a statistically significant difference. Due to the restricted measurement time, it was impossible to scan along the estimated Bragg peak position. This led to a placement of the detector slightly in front of the Bragg peak. Nevertheless, the potential disadvantage of passive beam delivery systems, in terms of radiation quality, can not be seen here, and is not expected to be any more significant, if the measurement had been carried out in the center of the Bragg peak. However, the simulations strongly suggest to collect more statistics, such that the differences in the spectra also emerge in the measurements. Still, the differences are so small that they only appear when plotting the spectra with a logarithmic vertical axis and it is questionable if they are large enough to account for a difference in biological effect.

Measurements by Martino et al. [78] and Kase et al. [68] show a good agreement for the carbon ion plateau measurement. The position in front of the Bragg peak can not be directly compared to the cited measurements. The Monte-Carlo simulations for the actively delivered carbon ions agree in their shape, relative contributions of

fragments, and mean values to those presented in [79], where a different primary beam energy was simulated.

Further experiments should include measurements outside the primary beam path, e. g. on the beam axis, but several centimeters behind the Bragg peak, or at lateral positions. Here, the difference is expected to be more pronounced because of the absence of the primary beam. However, these measurements are expected to take a long time, as the fluence of these secondary particles is low compared to the fluence of the primary ions, and will be very demanding on the beam time schedule.

When measuring in the primary ion-beam path, pile-up is an issue that has to be addressed by reducing the particle fluence on the detector to about 1000 particles per second on the detector surface. At HIT, this is well below the usual beam current range, where high currents are needed for fast treatment times. Because of the lack of monitoring devices available at HIT for these currents, it is suggested to use a scintillator at least to inhibit data taking when the momentary particle rate is too high. It then should be possible to measure the number of extracted primary particles, thus normalizing the measurements on the scintillator signal instead of taking the number of events the TEPC has registered.

4 Conclusion, Outlook

Modern particle radiotherapy increasingly leaves the concept of dose as a quantity behind and attempts to describe the biological effect using more relevant and measureable quantities, from biologically effective dose towards cell survival rates. The treatment planning systems that optimize the beam parameters to obtain a certain dose distribution can in principle optimize for any quantity, because they only solve a purely mathematical problem. Thus, it is reasonable to let them optimize for reaching a given survival level, which is ideally a step function, zero in the target volume and unity elsewhere. This ultimate goal will never be reached due to the physical properties of dose deposition as described in previous chapters. However, models relating biological factors and their dependence on physical quantities and vice versa, e. g. the OER dependence on the LET, or the RBE dependence on LET, offers the possibility to approach this ultimate goal further than with today's dose planning concepts.

Needless to say that these models require thorough understanding and must be benchmarked with biological as well as physical experiments. For the latter, more sophisticated measurement techniques than the standard dose determinations are requested. As pointed out in sec. 2.1.2, there is a relation between LET and biological effect. Thus, detectors capable of measuring the LET or similar quantities like the lineal energy are invaluable tools for verifying such a relationship. Apart from passive detectors like the fluorescent nuclear track detectors or track etched detectors, active detectors using silicon technology are promising candidates. Silicon diodes can also be operated as microdosimeters [80] and can be integrated into very small detectors, and TimePix sensors offer a variety of spectroscopic possibilities [81].

But also the tissue-equivalent proportional counter that was used in this work is, even though the underlying technology is already 50 years old, still an appropriate tool to access the radiation quality in terms of lineal energy. Aside from collecting more statistics, more measurements are proposed, e. g. to assess the microdosimetric properties of oxygen and helium beams, as well as changes in the spectra, if the beam has to traverse metal implants or bony structures.

Acknowledgments

I would like to thank all the people that supported me in the three years of my doctoral research.

- Joachim Ullrich for the very helpful questions and suggestions
- Michael Holzscheiter for the outstanding support in every respect
- Oliver Jäkel for the quick and detailed help in any problem
- Armin Lühr from Oncoray and Niels Bassler from Aarhus University, for the useful discussions about LET and its optimization
- Frank Wissmann and Thorsten Klages from PTB for their useful advice and filling the TEPC
- Chiara La Tessa from GSI for her great help in my early stages in the field of microdosimetry and for assisting with the troubleshooting in my equipment
- Lucas Buringo from FIAS for the productive discussions about microdosimetric Monte-Carlo simulations
- My colleagues and friends at Max-Planck-Institut, at DKFZ, and HIT, for their useful comments, questions, and the cheerful time we have spent together
- My family: Brigitte, Peter, Sonja, Sebastian and my grandparents for their lifetime support and asking helpful questions in layman's terms
- All my friends
- And all the others which I have forgotten to mention.

Vielen Dank an Euch alle!

Bibliography

[1] Becker, N. & Wahrendorf, J. *Krebsatlas der Bundesrepublik Deutschland 1981-1990. Atlas of Cancer Mortality in the Federal Republic of Germany* (Springer, Berlin Heidelberg New York, 1998). URL `http://www.krebsatlas.de`. Updated online.

[2] Baras, N. *et al.* *Krebs in Deutschland 2007/2008.*, vol. 8 (Robert Koch-Institut and Gesellschaft der epidemiologischen Krebsregister in Deutschland e.V. Berlin, 2012).

[3] LaFond, R. E. (ed.) *Cancer* (Oxford University Press, Oxford; New York, 2012), 3 edn.

[4] Bleif, M. *Krebs* (Klett-Cotta, Stuttgart, 2013).

[5] Radiation therapy answers: About radiation therapy. online. URL `http://www.rtanswers.org/statistics/aboutradiationtherapy/`. Retrieved 2013/09/16.

[6] Particle Therapy Co-operative Group (PTCOG). Statistics of patients treated in hadron therapy centers worldwide. online (2013). URL `http://ptcog.web.psi.ch/patient_statistics.html`. Retrieved 2013/09/16.

[7] Bethe, H. Zur Theorie des Durchgangs schneller Korpuskularstrahlen durch Materie. *Ann Phys* **397**, 325–400 (1930).

[8] International Commission on Radiation Units and Measurements. *Stopping Powers and Ranges for Protons and Alpha Particles.* ICRU Report No. 49 (1993).

[9] International Commission on Radiation Units and Measurements. *Stopping of Ions Heavier than Helium.* ICRU Report No. 73 (2005).

[10] International Commission on Radiation Units and Measurements. *Prescribing, Recording, and Reporting Proton-Beam Therapy.* ICRU Report No. 78 (2007).

[11] Douglas, B. & Fowler, J. The effect of multiple small doses of X rays on skin reactions in the mouse and a basic interpretation. *Radiat Res* **66**, 401–426 (1976).

[12] Grassberger, C., Trofimov, A., Lomax, A. & Paganetti, H. Variations in linear energy transfer within clinical proton therapy fields and the potential for biological treatment planning. *Int J Radiat Oncol* **80**, 1559–1566 (2011).

[13] Scholz, M. & Elsässer, T. Biophysical models in ion beam radiotherapy. *Adv Space Res* **40**, 1381–1391 (2007).

[14] Kase, Y. *et al.* Microdosimetric measurements and estimation of human cell survival for heavy-ion beams. *Radiat Res* **166**, 629–638 (2006).

[15] Schlegel, W. If you can't see it, you can miss it: the role of biomedical imaging in radiation oncology. *Radiat Prot Dosim* **139**, 321–326 (2010).

[16] Jäkel, O., Jacob, C., Schardt, D., Karger, C. P. & Hartmann, G. H. Relation between carbon ion ranges and x-ray ct numbers. *Med Phys* **28**, 701–703 (2001).

[17] Telsemeyer, J. *Investigation of an amorphous silicon flat-panel detector for ion radiography.* Ph.D. thesis, Universität Heidelberg (2012). URL `http://www.ub.uni-heidelberg.de/archiv/13590`.

[18] Rinaldi, I. *Investigation of novel imaging methods using therapeutic ion beams.* Ph.D. thesis, Universität Heidelberg (2011). URL `http://www.ub.uni-heidelberg.de/archiv/12605`.

[19] Min, C.-H., Kim, C. H., Youn, M.-Y. & Kim, J.-W. Prompt gamma measurements for locating the dose falloff region in the proton therapy. *Appl Phys Lett* **89** (2006).

[20] Testa, E. *et al.* Dose profile monitoring with carbon ions by means of prompt-gamma measurements. *Nucl Instrum Meth B* **267**, 993–996 (2009).

[21] Gwosch, K. *et al.* Non-invasive monitoring of therapeutic carbon ion beams in a homogeneous phantom by tracking of secondary ions. *Phys Med Biol* **58**, 3755–3773 (2013).

[22] Sellner, S., Welsch, C. P. & Holzscheiter, M. Real-time imaging of antiprotons stopping in biological targets – novel uses of solid state detectors. *Radiat Meas* **46**, 1770–1772 (2011).

[23] Parodi, K. *et al.* PET imaging for treatment verification of ion therapy: Implementation and experience at GSI Darmstadt and MGH Boston. *Nucl Instrum Meth A* **591**, 282–286 (2008).

[24] Enghardt, W. *et al.* Charged hadron tumour therapy monitoring by means of PET. *Nucl Instrum Meth A* **525**, 284–288 (2004).

[25] Knopf, A., Parodi, K., Bortfeld, T., Shih, H. A. & Paganetti, H. Systematic analysis of biological and physical limitations of proton beam range verification with offline PET/CT scans. *Phys Med Biol* **54**, 4477–4495 (2009).

[26] Knopf, A.-C. & Lomax, A. In vivo proton range verification: a review. *Phys Med Biol* **58**, R131 (2013).

[27] Horsman, M. R., Mortensen, L. S., Petersen, J. B., Busk, M. & Overgaard, J. Imaging hypoxia to improve radiotherapy outcome. *Nat Rev Clin Oncol* **9**, 674–687 (2012).

[28] Barendsen, G. W. *et al.* The effect of oxygen on impairment of the proliferative capacity of human cells in culture by ionizing radiations of different let. *Int J Radiat Biol* **10**, 317–327 (1966).

[29] Furusawa, Y. *et al.* Inactivation of aerobic and hypoxic cells from three different cell lines by accelerated ^{3}He-, ^{12}C- and ^{20}Ne-ion beams. *Radiat Res* **154**, 485–496 (2000).

[30] Bassler, N., Jäkel, O., Søndergaard, C. S. & Petersen, J. B. Dose- and LET-painting with particle therapy. *Acta Oncol* **49**, 1170–1176 (2010).

[31] Bassler, N. *et al.* LET-painting increases tumour control probability in hypoxic tumours. *Acta Oncol* 1–8 (2013).

[32] Lea, D. E. *Actions of Radiations on Living Cells* (Cambridge University Press, London, 1946).

[33] International Commission on Radiation Units and Measurements. *Linear Energy Transfer*. ICRU Report No. 16 (1970).

[34] Sørensen, B. S., Overgaard, J. & Bassler, N. In vitro RBE-LET dependence for multiple particle types. *Acta Oncologica* **50**, 757–762 (2011).

[35] Wenzl, T. & Wilkens, J. J. Modelling of the oxygen enhancement ratio for ion beam radiation therapy. *Phys Med Biol* **56**, 3251 (2011).

[36] Tegami, S. *LET measurements with a Liquid Ionization Chamber*. Ph.D. thesis, Universität Heidelberg (2013). URL `http://www.ub.uni-heidelberg.de/archiv/14675`.

[37] Fleischer, R. L., Price, P. B. & Walker, R. M. *Nuclear track in solids: principles and applications.* (University of California Press, 1975).

[38] Jadrníčková, I. *Spectrometry of linear energy transfer: Use in radiotherapy and radiation protection in high-energy particle fields*. Ph.D. thesis (2010). Germany: Lambert Academic Publishing.

[39] Pachnerová Brabcová, K., Ambrožová, I., Kolísková, Z. & Malušek, A. Uncertainties in linear energy transfer spectra measured with track-etched detectors in space. *Nucl Instrum Meth A* **713**, 5–10 (2013).

[40] Akselrod, M. S. & Sykora, G. J. Fluorescent nuclear track detector technology – A new way to do passive solid state dosimetry. *Radiat Meas* **46**, 1671–1679 (2011).

[41] International Commission on Radiation Units and Measurements. *Prescribing, Recording, and Reporting Photon Beam Therapy*. ICRU Report No. 50 (1993).

[42] Krämer, M. *et al.* Treatment planning for heavy-ion radiotherapy: physical beam model and dose optimization. *Phys Med Biol* **45**, 3299 (2000).

[43] Krämer, M. & Scholz, M. Treatment planning for heavy-ion radiotherapy: calculation and optimization of biologically effective dose. *Phys Med Biol* **45**, 3319 (2000).

[44] Horcicka, M., Meyer, C., Buschbacher, A., Durante, M. & Krämer, M. Algorithms for the optimization of rbe-weighted dose in particle therapy. *Phys Med Biol* **58**, 275 (2013).

[45] Scifoni, E. *et al.* Including oxygen enhancement ratio in ion beam treatment planning: model implementation and experimental verification. *Phys Med Biol* **58**, 3871 (2013).

[46] Ling, C. *et al.* Towards multidimensional radiotherapy (MD-CRT): biological imaging and biological conformality. *Int J of Radiat Oncol* **47**, 551–560 (2000).

[47] Tanderup, K., Olsen, D. R. & Grau, C. Dose painting: Art or science? *Radiother Oncol* **79**, 245–248 (2006).

[48] Thorwarth, D., Soukup, M. & Alber, M. Dose painting with IMPT, helical tomotherapy and IMXT: A dosimetric comparison. *Radiother Oncol* **86**, 30–34 (2008).

[49] Krämer, M. & Jäkel, O. Biological dose optimization using ramp-like dose gradients in ion irradiation fields. *Phys medica* **21**, 107–111 (2005).

[50] Fassò, A., Ferrari, A., Ranft, J. & Sala, P. FLUKA: A multi-particle transport code. *CERN-2005-10* (2005).

[51] Battistoni, G. *et al.* The FLUKA code: description and benchmarking. *AIP Conf Proc* **896**, 31–49 (2007).

[52] Holzscheiter, M. H. *et al.* The biological effectiveness of antiproton irradiation. *Radiother Oncol* **81**, 233–242 (2006).

[53] Kavanagh, J. N. *et al.* Antiproton induced DNA damage: proton like in flight, carbon-ion like near rest. *Sci Rep* **3**, 1–10 (2013).

[54] Rossi, H. H. *Microscopic energy distribution in irradiated matter. In: "Radiation Dosimetry"* (New York: Academic Press, 1968).

[55] Brenner, D. J. & Hall, E. J. Secondary neutrons in clinical proton radiotherapy: A charged issue. *Radiotherapy and Oncology* **86**, 165–170 (2008).

[56] Rossi, H. H. & Zaider, M. *Microdosimetry and Its Applications* (Springer, Berlin Heidelberg New York, 1995).

[57] Fano, U. Note on the Bragg-Gray cavity principle for measuring energy dissipation. *Radiat Res* **1**, 237–240 (1954).

[58] Kliauga, P., Waker, A. & Barthe, J. Design of tissue-equivalent proportional counters. *Radiat Prot Dosim* **61**, 309–322 (1995).

[59] Kellerer, A. M. An assessment of wall effects in microdosimetric measurements. *Radiat Res* **47**, 377–386 (1971).

[60] Hawkins, R. A statistical theory of cell killing by radiation of varying linear energy transfer. *Radiat Res* **140**, 366–374 (1994).

[61] Hawkins, R. A microdosimetric-kinetic model of cell death from exposure to ionizing radiation of any LET, with experimental and clinical applications. *Int J Radiat Biol* **69**, 739–755 (1996).

[62] Hawkins, R. B. A microdosimetric-kinetic theory of the dependence of the RBE for cell death on LET. *Med Phys* **25**, 1157–1170 (1998).

[63] Hawkins, R. B. A microdosimetric-kinetic model for the effect of non-poisson distribution of lethal lesions on the variation of RBE with LET. *Radiat Res* **160**, 61–69 (2003).

[64] Inaniwa, T. *et al.* Treatment planning for a scanned carbon beam with a modified microdosimetric kinetic model. *Phys Med Biol* **55**, 6721–6737 (2010).

[65] Kellerer, A. M. & Rossi, H. H. The theory of dual radiation action. *Curr Top Radiat Res* **8**, 85–158 (1972).

[66] Curtis, S. B. Lethal and potentially lethal lesions induced by radiation — a unified repair model. *Radiat Res* **106**, 252–270 (1986).

[67] Tobias, C. A. The repair-misrepair model in radiobiology: Comparison to other models. *Radiat Res* **104**, 77–95 (1985).

[68] Kase, Y. *et al.* Microdosimetric approach to NIRS-defined biological dose measurement for carbon-ion treatment beam. *J Radiat Res* **52**, 59–68 (2011).

[69] Inaniwa, T. *et al.* Effects of dose-delivery time structure on biological effectiveness for therapeutic carbon-ion beams evaluated with microdosimetric kinetic model. *Radiat Res* **180**, 44–59 (2013).

[70] International Commission on Radiation Units and Measurements. *The Quality Factor in Radiation Protection.* ICRU Report No. 40 (1986).

[71] International Commission on Radiation Protection. 1990 recommendations of the international commission on radiological protection. *Annals of the ICRP* **21** (1991).

[72] Rossi, H. H. & Rosenzweig, W. A device for the measurement of dose as a function of specific ionization. *Radiology* **64**, 404–411 (1955).

[73] Shonka, R. F., Rose, J. E. & Failla, G. Conducting plastic equivalent to tissue, air and polystyrene. *Second United Nations International Conference on Peaceful Uses of Atomic Energy* 160 (1958).

[74] Schrewe, U., Brede, H., Pihet, P. & Menzel, H. On the calibration of tissue-equivalent proportional counters with built-in alpha particle sources. *Radiat Prot Dosim* **23**, 249–252 (1988).

[75] Berger, M., Coursey, J., Zucker, M. & Chang, J. ESTAR, PSTAR, and ASTAR: Computer programs for calculating stopping-power and range tables

for electrons, protons, and helium ions (version 1.2.3). Online (2013). URL `http://physics.nist.gov/Star`. Retreived 09/02/2013.

[76] Parodi, K. *et al.* Monte carlo simulations to support start-up and treatment planning of scanned proton and carbon ion therapy at a synchrotron-based facility. *Phys Med Biol* **57**, 3759 (2012).

[77] Böhlen, T. T., Dosanjh, M., Ferrari, A., Gudowska, I. & Mairani, A. FLUKA simulations of the response of tissue-equivalent proportional counters to ion beams for applications in hadron therapy and space. *Phys Med Biol* **56**, 6545 (2011).

[78] Martino, G., Durante, M. & Schardt, D. Microdosimetry measurements characterizing the radiation fields of 300 MeV/u ^{12}C and 185 MeV/u ^{7}Li pencil beams stopping in water. *Phys Med Biol* **55**, 3441–3449 (2010).

[79] Böhlen, T. T., Dosanjh, M., Ferrari, A. & Gudowska, I. Simulations of microdosimetric quantities with the monte carlo code FLUKA for carbon ions at therapeutic energies. *Int J Radiat Biol* **88**, 176–182 (2012).

[80] Rosenfeld, A. *et al.* A new silicon detector for microdosimetry applications in proton therapy. *IEEE T Nucl Sci* **47**, 1386–1394 (2000).

[81] Granja, C., Jakubek, J., Platkevic, M., Pospisil, S. & Vykydal, Z. Detection and real time spectroscopy of charged particles with the timepix pixel detector. *AIP Conf Proc* **1204**, 75–79 (2010).

Nomenclature

CT	Computed Tomography. Using mathematical algorithms, the information from X-ray photon attenuation for different angles is transformed into a three-dimensional electron density image of the patient.
DNA	Deoxyribonucleic acid, the molecule encoding the genetic information of living organisms
HIT	Heidelberg Ion Beam Therapy Center. Patients are treated with protons and carbon ions. Research is also possible with other ions, e.g. oxygen.
IMRT	Intensity modulated radiotherapy. Not only the shape of each of the 6–8 fields is modulated, but also the photon fluences and thus the dose, resulting in the possibility to restrict the high-dose volume to complex-shaped, even to concave-shaped, tumors.
LEM	Local Effect Model, relating the very high local doses in close vicinity to a track of a charged particle to the according surviving fraction at that dose level, resulting in a RBE when compared to the survival fraction for the same dose of a reference radiation.
LET	Linear energy transfer, also called restricted stopping power. It is a measure of the ionization density along a single particle track.
MKM	Microdosimetric Kinetic Model. A model that relates microdosimetric quantities such as the dose mean lineal energy to the relative biological effectiveness (RBE).
MRI	Magnetic Resonance Imaging. Like CT, it is used for imaging patients. However, rather than X-ray attenuation, the technique uses the nuclear magnetic resonance as imaging information. Compared to

CT, the contrast in soft tissue is better, which makes MRI a valuable tool to gain additional information about tumors and their surroundings.

OER — Oxygen enhancement ratio. The factor of additional dose needed to kill cells when they are provided with little or no oxygen.

PET — Positron emission tomography. A radioactive substance undergoing β^+ decay with short lifetime is attached to a specific molecule, e.g. a sugar. The two 511 keV photons from the positron annihilation are detected and their line of origin reconstructed. The accumulation point of line crossings corresponds to the volume in which the substance has accumulated. In the case of sugar, it represents an area of high cellular activity.

RBE — Relative biological effectiveness, the ratio of a dose in investigation and a reference dose, both leading to the same biological effect.

SOBP — Spread out Bragg peak. It is a superposition of several Bragg peaks in longitudinal direction to achieve a constant high dose spread over a larger volume, e.g. the tumor.

VMAT — Volumetric modulated arc therapy. It is a method developed by the manufacturer Elekta and can be understood as an improved version of IMRT. Different from the step-and-shoot-technique in IMRT, where the fields are applied one after the other, the irradiation is delivered while the treatment head is rotating around the patient with different rotational velocities and continuously moving collimators. Furthermore, the dose rate is changed along the rotation to achieve the planned dose distribution, which the manufacturer promotes to be superior to those gained by IMRT.